

Institut für Photogrammetrie
und Geoinformation

GFZ

Helmholtz-Zentrum
P O T S D A M

Leibniz University Hannover
Institut für Photogrammetrie und Geoinformation

Helmholtz Centre Potsdam, German Research Center for
Geosciences (GFZ)

Master Thesis

Radar Remote Sensing Observations to Investigate Slow- Moving Landslides

Author: Hasan Sharifi

Matri. No. 10008693

Supervisors: Prof. Dr. Mahdi Motagh

Dr. –Ing. Sanaz Vajedian

Potsdam, April 2019

Declaration of Authorship

I hereby declare the work presented in this master thesis has been composed by me. All the consulted published or unpublished works have been cited clearly throughout the thesis. I confirm that no sources or works other than those listed in the bibliography have been used. In additions, this master thesis has not been submitted to any other degree examinations.

Hasan Sharifi

Signature:

Potsdam, 23.04.2019

Eidesstattliche Erklärung

Ich erkläre hiermit, die Arbeit selbständig verfasst zu haben und keine anderen als die angegebenen Quellen und Hilfsmittel benutzt zu haben. Alle Stellen der Arbeit, die wörtlich oder sinngemäß aus anderen Quellen übernommen wurden, habe ich als solche kenntlich gemacht. Die Arbeit wurde in gleicher oder ähnlicher Form noch keiner Prüfungsbehörde vorgelegt.

Hasan Sharifi

Unterschrift:

Potsdam, 23.04.2019

Abstract

The northern part of Nepal is located on Himalaya Mountains and is prone to have a lot of rain-induced landslides. Assessing the kinematics of landslides in those areas is an important topic to better understand landslide processes and mitigate hazards associated with them. The study area in this research consists of 3 landslides in Annapurna range of the Himalayas close to the Nepal-China border. The aim of the study is to evaluate the potential of SAR data for deriving the kinematics of landslides in this region. In order to achieve this goal, the InSAR (Interferometric Synthetic-Aperture Radar) technique has been implemented utilizing data from ALOS-1 satellite between the years 2007-2011 and from Sentinel-1 satellite between 2014 and 2016. Ground surface deformation is analyzed by performing the PSI (Persistent Scatterers Interferometry) time-series analysis approach to derive ground deformation and velocity in line-of-sight (LOS) direction from the satellite to the ground.

To better evaluate the kinematics of landslides, LOS motions derived from InSAR analysis are projected to the motion along the slope direction considering the area's local topography and satellite's incidence and heading angle parameters. Moreover, a post-processing strategy is implemented and the points with higher sensitivity to the satellite's acquisition geometry are considered for final ground surface deformation map which produces better and more accurate results. Furthermore, the final results are classified into clusters of points to assess the behavior of slow moving landslides with millimeter accuracy.

Keywords: Slow-moving landslide, InSAR, ALOS-1, Sentinel-1, Time-series analysis

Table of Contents

Abstract	2
List of Figures.....	5
1 Introduction	8
1.1 Motivation	10
1.2 The Study Area.....	10
1.2.1 Landslide in Northern Nepal	10
1.3 Task Description	11
1.4 Related Work	12
2 Theoretical Background	14
2.1 Synthetic Aperture Radar (SAR).....	14
2.1.1 SAR Data Acquisition	14
2.1.2 The SAR Image.....	17
2.2 SAR Interferometry.....	18
2.2.1 Introduction.....	18
2.2.2 SAR Interferometric Process	20
2.3 Time Series Analysis.....	26
2.3.1 Persistent Scatterers Interferometry (PSI).....	26
2.3.2 Small Baseline Subset Interferometry (SBAS)	29
3 Methodology.....	31
4 Data overview	35
4.1 SAR Data Processing Software and Programming Languages.....	38
5 Implementation	39
5.1 ALOS-1 Persistent Scatters Interferometry	39
5.2 Sentinel-1 Persistent Scatterer Interferometry.....	45
5.3 LOS Velocity Project to Slope Displacement	53
5.3.1 ALOS-1 Slope Displacement	54
5.3.2 Sentinel-1 Slope Displacement.....	56
5.4 Clustering and Classification of Slope Displacement Maps.....	57
5.4.1 Kernel Density Estimation	58
5.4.2 Clustering of ALOS-1 Slope Displacement Map	59
5.4.3 Clustering of Sentinel-1 Slope Displacement Map.....	60

6	Conclusion and Outlook.....	62
7	References	64

List of Figures

Figure 1-1: Global Landslide Susceptibility Map	8
Figure 1-2: Global Topography Map. Source: “OpenStreetMap”	9
Figure 1-3: The location of Landslides in Nepal. The three polygons show the landslide boundaries.....	11
Figure 2-1: SAR Image Acquisition Geometry. Source: ESA earth online	15
Figure 2-2: SAR Image Acquisition Geometry from the side view. Source: ESA earth online .	15
Figure 2-3: Penetration of different wavelengths. Source: Nasa, (Podest, 2017).	16
Figure 2-4: Sentinel-1 Intensity Image of Mazari Sharif (Afghanistan).....	18
Figure 2-5: Across-track interferometry to explain the phase difference. Source: (Bamler & Hartl, 1998).....	19
Figure 2-6: Deformation “d” between two SAR image acquisition. Source: (Crosetto et al., 2016).....	20
Figure 2-7: Interferometric process of SAR Images	21
Figure 2-8: The left figure is the Master Intensity Image and the right figure is the Slave Intensity Image from Sentinel-1.....	22
Figure 2-9: The left figure is a STRM-1 Digital Elevation Model and the right figure shows the initial interferogram product.	22
Figure 2-10: The flattened Interferogram after topographic phase removal.....	23
Figure 2-11: The left image shows the estimated coherence values with the black color as 0 and white color as 1 values. The image on the right represents the filtered interferogram based on Goldstein filtering method.	24
Figure 2-12: The left figure shows the refined filtered interferogram. The right figure indicates the refined unwrapped phase.	26
Figure 2-13: Persistent Scatterers Interferometry (PSI) algorithm steps.	27
Figure 2-14: Amplitude Dispersion Index (Ferretti et al., 2001)	28
Figure 2-15: Small Baseline Subset Interferometry (SBAS) algorithm steps.....	29
Figure 3-1: Methodology flowchart for post-processing of the LOS displacement velocity results.....	31
Figure 3-2: Aspect Map of the study area. The unit is “degree”.	32
Figure 3-3: Slope Map of the study area. The unit is “degree”	33
Figure 3-4: Sensitivity Map of InSAR measurement to slope displacement.....	34
Figure 4-1: SAR Satellite Missions. (UNAVCO)	35
Figure 4-2: ESA Earth Online access hub for downloading Sentinel-1 SAR data.	36
Figure 4-3: Vertex portal of Alaska Satellite Facility to download Sentinel-1 SAR dat.....	37
Figure 5-1: Intensity Image of the ALOS-1 data. The figure on the left is the original data. The figure on the right is the resampled subset covering the study area.....	39
Figure 5-2: PSI time series network of slave images w.r.t. the master image shown with yellow point.....	41
Figure 5-3: ALOS-1 SAR intensity average image	41
Figure 5-4: The generated interferograms for ALOS-1 data w.r.t. the super master image (01.23.2009)	42

Figure 5-5: Multi-temporal coherence with white color indicating perfect PS model fit..... 43

Figure 5-6: PSI average LOS displacement velocity map for the first landslide area. The unit is in mm/year..... 44

Figure 5-7: PSI average LOS displacement velocity map for the second landslide area. The unit is in mm/year. 45

Figure 5-8: PSI average LOS displacement velocity map for the first landslide area. The unit is in mm/year..... 45

Figure 5-9: Intensity Image of the Sentinel-1 data. The figure on the left is the original data. The figure on the right is the resampled subset covering the study area. 46

Figure 5-10: PSI time series network of slave images w.r.t. the master image shown with yellow point..... 48

Figure 5-11: Sentinel-1 SAR intensity average image 48

Figure 5-12: The generated interferograms for Sentinel-1 data w.r.t. the super master image (21.03.2015) 49

Figure 5-13: Multi-temporal coherence with white color indicating perfect PS model fit. 50

Figure 5-14: PSI average LOS displacement velocity map for the first landslide area. The unit is in mm/year..... 50

Figure 5-15: PSI average LOS displacement velocity map for the second landslide area. The unit is in mm/year. 51

Figure 5-16: PSI average LOS displacement velocity map for the third landslide area. The unit is in mm/year..... 51

Figure 5-17: Number of points obtained in the first landslide area for every LOS velocity interval. The blue line indicates the ALOS-1 and the orange line indicates the Sentinel-1 data sets. 52

Figure 5-18: Number of points obtained in the second landslide area for every LOS velocity interval. The blue line indicates the ALOS-1 and the orange line indicates the Sentinel-1 data sets. 52

Figure 5-19: Number of points obtained in the third landslide area for every LOS velocity interval. The blue line indicates the ALOS-1 and the orange line indicates the Sentinel-1 data sets. 52

Figure 5-20: ALOS-1 slope displacement map for the first landslide area..... 54

Figure 5-21: ALOS-1 slope displacement map for the second landslide area. 55

Figure 5-22: ALOS-1 slope displacement map for the third landslide area. 55

Figure 5-23: Sentinel-1 slope displacement map for the first landslide area..... 56

Figure 5-24: Sentinel-1 slope displacement map for the second landslide area..... 56

Figure 5-25: Sentinel-1 slope displacement map for the third landslide area. 57

Figure 5-26: The figure on the left shows the kernel density estimation map of hotspot clusters. The clusters with high density have bright color. The figure on the right shows the slope displacement map after removing the low density cluster of points. 59

Figure 5-27: The left figure indicates the time series of a point in the blue rectangle cluster. The right figure indicates the time series of a point in the green rectangle cluster. 59

Figure 5-28: The figure on the left shows the kernel density estimation map of hotspot clusters. The clusters with high density have bright color. The figure on the right shows the slope displacement map after removing the low density cluster of points. 60

Figure 5-29: The left figure indicates the time series of a point in the blue rectangle cluster. The right figure indicates the time series of a point in the green rectangle cluster. 61

1 Introduction

Landslides have been always considered as important natural hazards and disaster phenomena which can bring about massive destruction in earth surface, infrastructure and are responsible for a large number of human casualties. The landslides create a form of ground movement which happen as a process in which the earth's gravity causes the movements of the earth surface masses such as rocks and soil towards the slope direction of the hills and mountains. Within this phenomenon, the earth surface masses may go down the hill slopes suddenly or they can slide in a rate of couple of centimeters per year caused by natural events or human activities in the environment. In all of those cases, the gravity of the earth plays an important role in the landslide formation with its influence over the earth surface.

According to the information provided by NASA Earth Observatory, the landslides triggered by heavy rain kill roughly 4600 people each year. In this case, the major factors of making an area susceptible to the landslides are high elevation and steep slopes, deforestation, presence of roads and the location of faults. In the following figure, a global map of the landslide susceptibility is provided (Stanley & Kirschbaum, 2017).

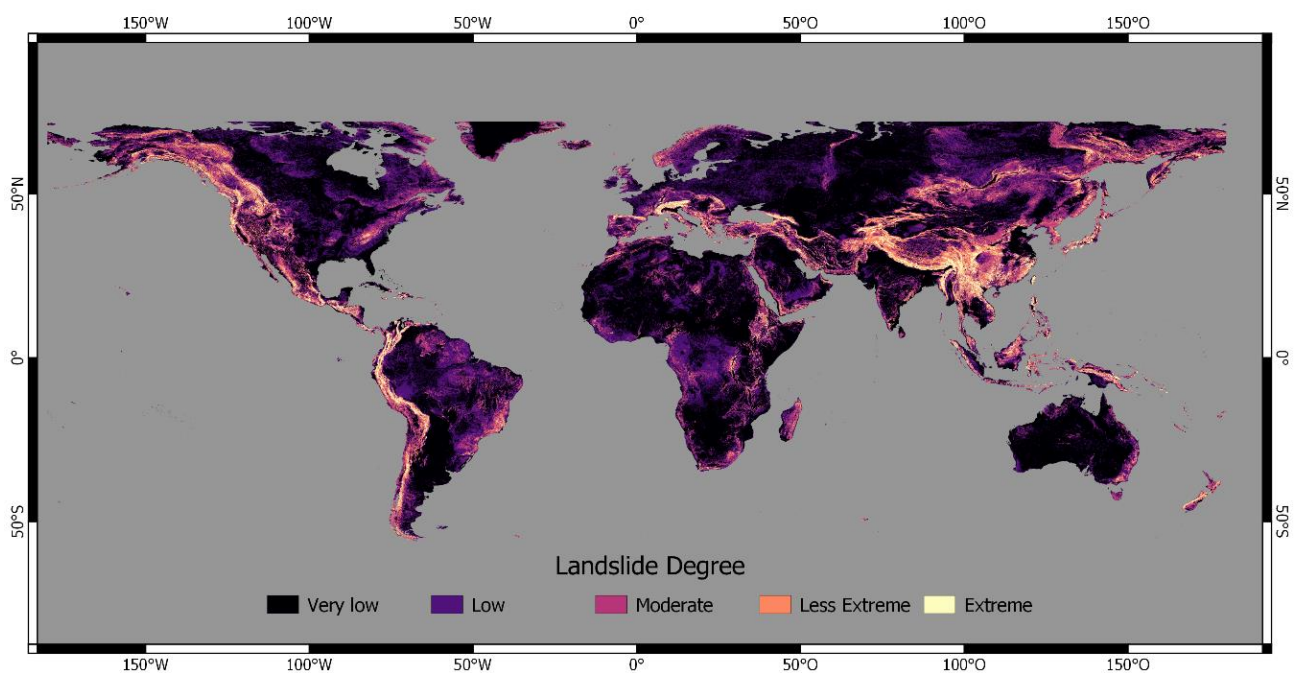


Figure 1-1: Global Landslide Susceptibility Map

According to the information in the above figure, landslides have a major effect on the Western parts of the North and South America as well as the South and Eastern Asia. In most of those regions, landslides occur on the mountainous areas which are counted as treats for the local population living in the foothill zones and the infrastructure. In the following figure, the world topography map from the “Open Street Map” data is shown accordingly.

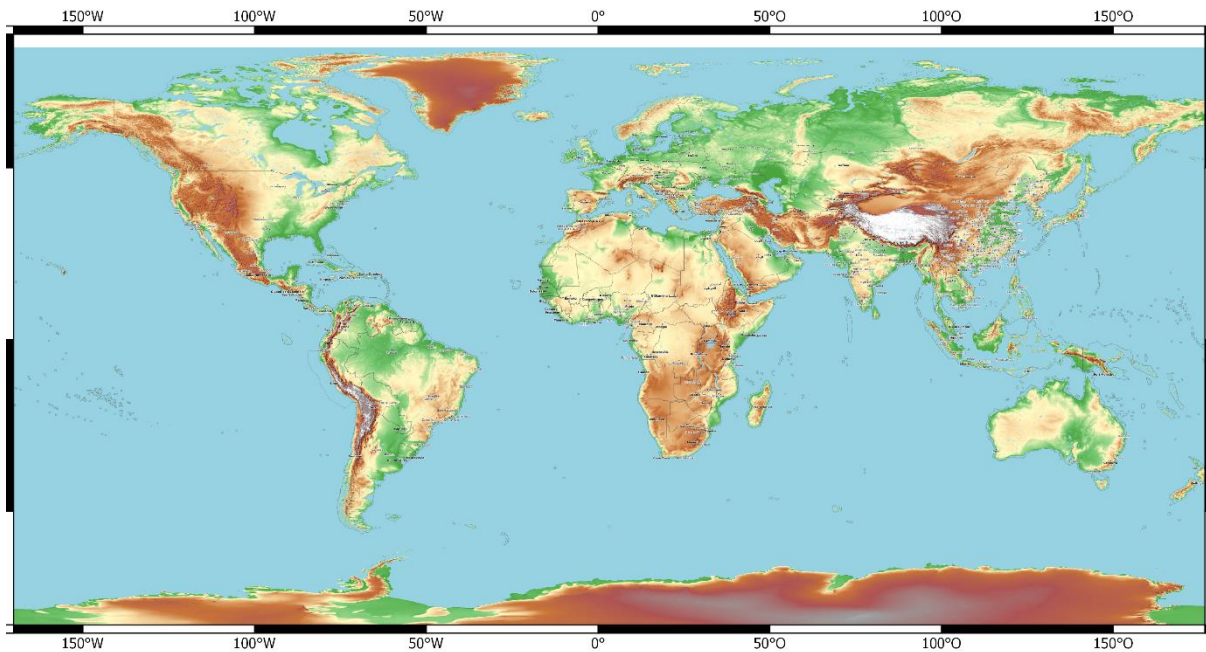


Figure 1-2: Global Topography Map. Source: “OpenStreetMap”

Analyzing and studying the characteristics of landslides would result in better understanding their behavior and enables to monitor and mitigate the hazards and damages related to them. For this purpose, many geodetic techniques such as Global Positioning System (GNSS) for a pointwise deformation measurement are actively used which provide up to millimeter (mm) accuracy for the ground movement and landslide applications (Mirzaee, Motagh, & Akbari, 2017). The other techniques include ground-based observation systems which provide also high accuracy measurement results on-site (Motagh et al., 2015).

From the other side, Interferometric Synthetic Aperture Radar Interferometry (InSAR) has been a widely used space geodetic technique that takes the earth surface observations in all the weather conditions and provides high spatial and temporal resolution radar images. This space geodetic technique is more efficient for large scale measurements for the purpose of slow-moving landslide and subsidence monitoring over large areas where the ground-based surveying techniques are difficult to be applied (Mirzaee, Motagh, & Akbari, 2017). Generally

the ground-based techniques provide point-wise measurements in the observation area which may not be suitable when analyzing spatially large areas (Motagh et al., 2015). In fact, with the availability of high quality data from numerous observatory satellites, the landslide analysis using InSAR has been more practical.

1.1 Motivation

The Synthetic Aperture Radar Interferometry (InSAR) space geodetic technique has developed since the last two decades as a powerful tool to measure the earth surface deformation using the satellites from space. This technique includes analyzing radar images acquired in different dates by the satellites from the same area on the Earth surface (Haghshenas Haghghi & Motagh, 2016). In fact, many different Earth surface deformation types such as slow-moving landslides, urban land subsidence, mining area subsidence, etc. including spatially small to relatively large areas such as thousands of kilometers could be observed using InSAR (Rott, Scheuchl, Siegel, & Grasmann, 1999).

The time series analysis techniques are developed in the field of InSAR with the increasing availability of radar images obtained by different satellites. These techniques are used to derive slow moving landslide deformation rates with an improvement in the temporal resolution (Motagh et al., 2015). The availability of high temporal and spatial resolution data such as Sentinel-1 mission Interferometric Wide Swath (IW) with 250 Km Swath coverage and 5x20 meters spatial resolution and 6 days temporal resolution enables more accurate and efficient deformation analysis for different applications.

1.2 The Study Area

1.2.1 Landslide in Northern Nepal

The study area consists of 3 landslides in Annapurna range of the Himalayas close to the Nepal-China border. Nepal is a country located with China to the North, India to the West, South and East. The latitude of this study area is between 29.22 and 29.3 degrees North and the Longitude between 83.95 and 84.09 degrees East, covering approximately 93 km². The area is very rich in terms of the bio-diversity and its unique geographical position with mostly

high altitude. The elevation of the study area ranges from 4500 meters to almost 5000 meters above the sea level. In this part of Nepal which the Himalayan Mountain is located, the vegetation is limited and the area is mostly covered by rocks and high slope mountains and is prone to have a lot of rain-induced landslides.

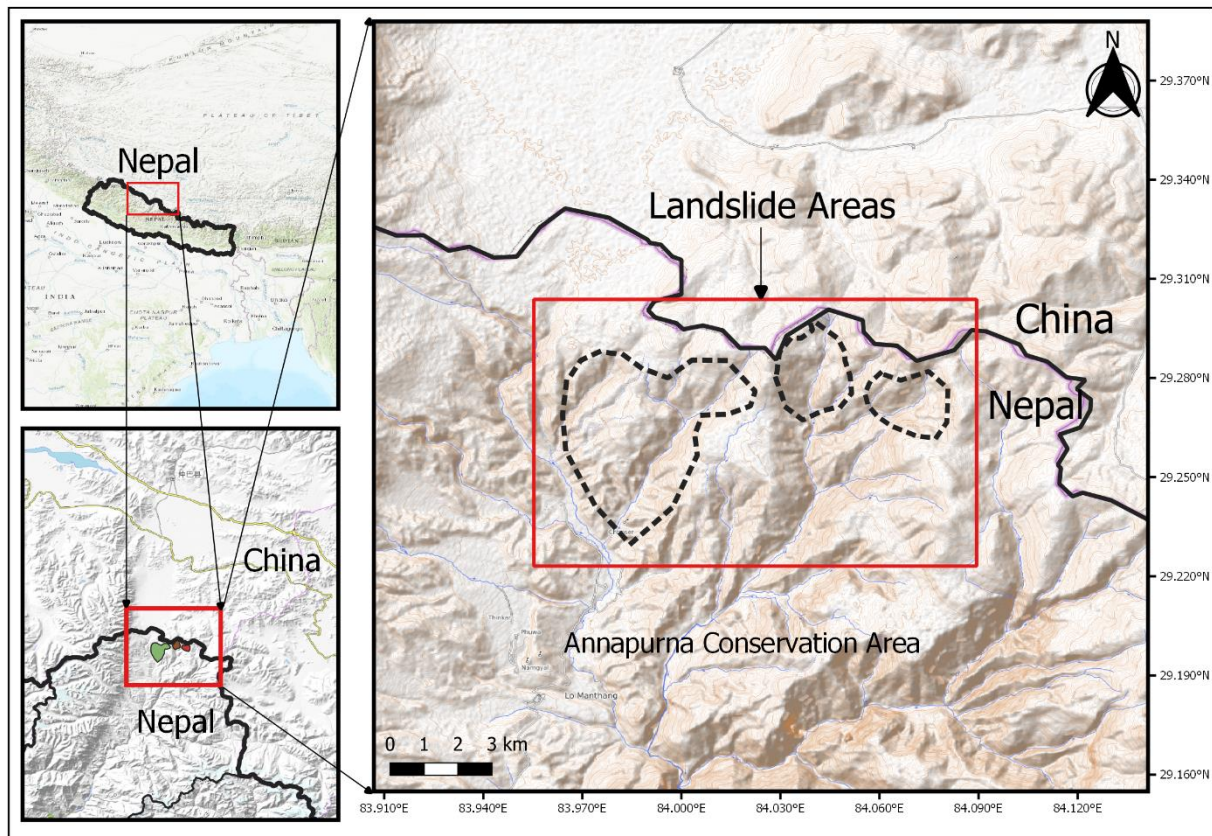


Figure 1-3: The location of Landslides in Nepal. The three polygons show the landslide boundaries.

1.3 Task Description

The aim of this thesis is to study the kinematics and characteristics of slow-moving landslides using Interferometric Synthetic Aperture Radar Interferometry (InSAR) technique. This technique allows identifying the ground displacement in the landslide areas for the goal of natural hazard assessment. The ground surface displacements are detected in millimeter level accuracy which proves to be an efficient geodetic observation technique. In the study area, datasets from ALOS-1 and Sentinel-1 satellites are used to perform time series analysis over different time intervals. As the study area is located in Himalayas with high slope topography, the Line of Sight (LOS) displacement values may not be perfectly representing the

true ground surface deformation in this area. Hence, the LOS displacement values towards and away from the satellite need to be projected into the direction of the local slope considering the acquisition geometry of the satellite with respect to the topography specifications. Therefore, the “aspect map” showing the direction of the slope in 360 orientation, the “slope map” representing the steepness of the local slope from 0 to 90 degrees are used together with the satellite’s incidence and heading angle values as parameters to create the “sensitivity map”. The generated sensitivity map contains an index for every point on the ground that allows us to obtain the displacement velocities in the direction of the slope with high sensitivity index in order to produce more accurate map of the real motion.

1.4 Related Work

There have been many works and approaches to monitor slow-moving landslides with the availability of more SAR data obtained by different satellite missions in the past two decades. The idea of using InSAR time series analysis such as Persistent Scatterer Interferometry (PSI) has been proposed by (Ferretti, Prati, & Rocca, 2001) and the Small Baseline Subset (SBAS) by (Berardino, Mora, Lanari, Sansosti, & Mallorqui, 2003). There are also some other approaches such as SqueeSAR (Ferretti et al., 2011) which helps improve the interferometric coherence based on statistical tests. These algorithms have paved the way for analyzing the kinematics of landslides.

One of the initial works to detect the dynamics of slow-moving landslides is by (Hilley, Bürgmann, Ferretti, Novali, & Rocca, 2004) using the Permanent Scatterer Analysis which the rates and variations in the rate of slow moving landslides has been studied. Their job has helped to understand the behavior of landslides over large areas and time spans.

One of the inspiring works has been done by (Haghshenas Haghghi & Motagh, 2016) to assess the ground surface displacement in Taihape landslide, New Zealand with Envisat (C-band) and TerraSAR-X (X-band) SAR Interferometry using SBAS time series analysis. Assuming the fact that landslide movement is driven by gravity and the geometry of the area’s slope plays an important role in the direction of the movement, they have attempted to assess the suitability of InSAR for the landslide. Therefore, they estimated the sensitivity of InSAR LOS

measurement to slope movement which has been used as a reference to generate such a sensitivity map for the two landslide case studies here.

Another approach to monitor landslide in Northern Iran Shabkola area using InSAR time-series analysis and GPS observations has been done by (Mirzaee et al., 2017) which the area is facing mass movements in the upstream. Several natural and human-made factors such as deforestation, land-use changes, steep slope, high precipitation rate and natural erosion have contributed to the landslide area as explained by their work. They have analyzed the relationship between the sensitivity of radar observations and geometric parameters to detect the displacement in the landslide area and both the velocity measurement by InSAR Line-of-Sight and GPS are projected to the slope direction using the sensitivity map. A significant result in their study is finding a previously unrecognized area with landslide located in a dense vegetation covered site using ALOS data time series analysis with long wavelength (L-band) which was observed by numerous cracks and scarps during a field survey later. In fact this proves the benefits of InSAR which is able to monitor over a relatively larger area compared to the GPS measurement which is mainly point-wise and limited to a specific area of interest.

Other related works could be mentioned as (Moretti et al., 2013) which landslide activity maps are generated using PSI approach to distinguish the active and inactive landslides. Furthermore many other works could be mentioned such as (Handwerger, Booth, Huang, Fielding, & Bürgmann, 2019) which have analyzed how a stable landslide leads to a major failure due to heavy rainfall by analyzing 8 years of stable sliding in Mud Creek landslide, California, USA. Hence, by looking at these works, the characteristics of slow-moving landslides in the case study of Northern Nepal regions are analyzed with scientific approaches using InSAR in this thesis. The proposed methods try to estimate more true and accurate estimation of the ground surface deformation in landslides.

2 Theoretical Background

2.1 Synthetic Aperture Radar (SAR)

As in the late 1970s when the spaceborne imaging radars became important in the remote sensing field (Bamler & Hartl, 1998), today the Synthetic Aperture Radar (SAR) plays a significant role in earth surface investigations. Synthetic Aperture Radar (SAR) is a spaceborne or airborne imaging system used for the purpose of the Earth surface mapping and environmental monitoring that produces high resolution remote sensing images. The images are generated using radar signals that can travel from the satellite to the earth in a long-range as the sensor sends the microwave signals to the ground and detects the backscattered waves reflected back. The SAR system takes advantage of the microwave radar signals to penetrate the clouds and operates in the day and night time and therefore it is not limited by the day time and atmospheric conditions. It is an active system that is not dependent on the sun illumination and can observe the earth surface regardless of the day and night time. Overall, the SAR system has the ability to generate high-resolution images regardless of the flight altitude and is not dependent on the weather since it can use different frequency range. The produced SAR images could be used in many remote sensing and mapping applications which some of them include monitoring the environmental changes such as deforestation, volcano monitoring, flood and earthquakes together with landslides and urban land subsidence.

2.1.1 SAR Data Acquisition

The SAR system produces 2-Dimensional images with the dimension along the flight track or direction called “azimuth”. The azimuth (along-track) describes the linear distance or image scale parallel to the flight direction. The other dimension across the track and perpendicular to the azimuth is called “range” which is also describes the distance from the radar to the target by the Line-of-Sight (LOS). The SAR image resolution in azimuth direction is constant and not dependent on the range. In the following figure, basic geometry of SAR image acquisition is shown.

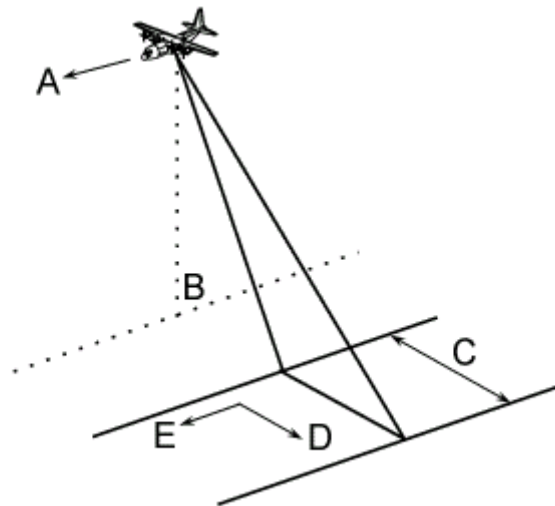


Figure 2-1: SAR Image Acquisition Geometry. Source: ESA earth online

As in the above figure, the azimuth and range dimensions are shown as 'E' and 'D' letters. The spaceborne or airborne system is flying in the direction 'A' with the nadir 'B' showing the flight trajectory under the sensor. Since SAR is a side-looking system, the microwaves beams are transmitted from the sensor to the ground covering a swath 'C' on the ground. In the following figure, the side profile of the SAR acquisition geometry is shown.

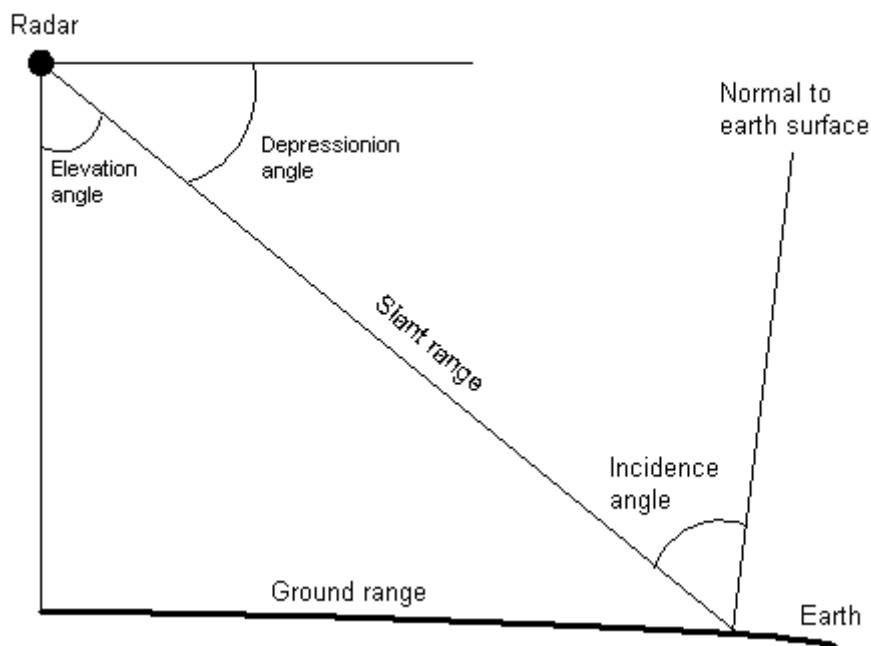


Figure 2-2: SAR Image Acquisition Geometry from the side view. Source: ESA earth online

The above figure describes how the microwave beam is transmitted from the sensor to the ground. The Slant Range is the distance travelled in the line-of-sight by the beam that creates the Depression angle between the line-of-sight and the horizontal plane of the sensor

platform. The angle between the line-of-sight and the nadir is known as Elevation angle and the angle with respect to the ground surface is the Incidence angle. Lastly, the Ground range indicates the true horizontal distance along the ground.

The microwave bands of the satellite SAR systems are currently in X, C, and L band which their characteristics are shown in the following table.

Microwave Band	Frequency (GHz)	Wavelength (cm)	Missions	Applications
X - Band	10	2.4 - 3.8	X-SAR	Agriculture, ocean, high resolution radar
C - Band	5.3	3.8 - 7.5	ERS, Envisat, Radarsat	Ocean, agriculture
L - Band	1.2	14 - 30	J-ERS, ALOS	Agriculture, forestry, soil moisture

Table 2-1: The used microwave bands. Source: DLR

If we show the wavelength as (λ), speed of light as (c) and frequency as (f), the wavelength is calculated as the following formula:

$$\lambda = \frac{c}{f} \tag{1}$$

According to the above formula, the higher frequency leads to a shorter wavelength and reversely, a lower frequency will lead to a longer wavelength. This point could be useful when considering the penetration of microwaves in the forests or areas with dense vegetation coverage. In fact, longer wavelength has more penetration power which is suitable to reach the earth surface in such areas. In the following figure, the penetration capability of each wavelength is shown.

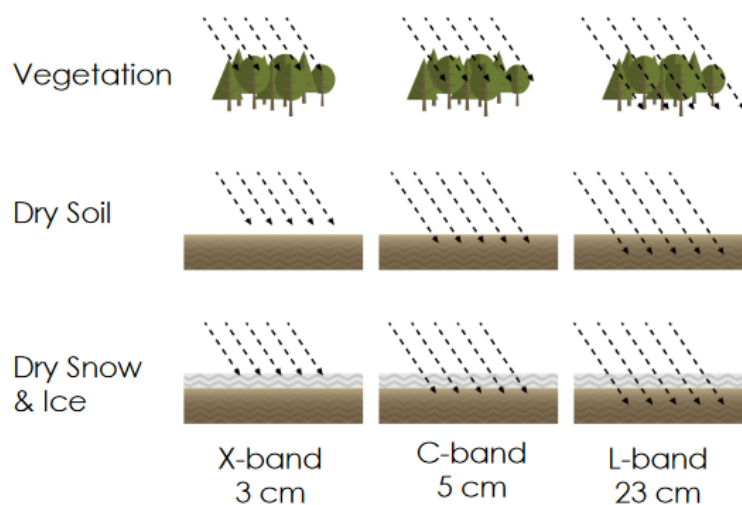


Figure 2-3: Penetration of different wavelengths. Source: Nasa, (Podest, 2017).

It could be inferred that different applications may require different wavelengths as L-band is mostly suitable for the forest, high vegetation areas and wetlands, and the X-band could be useful for dry lands such as urban areas.

2.1.2 The SAR Image

The SAR system measures the strength of the returned signal to determine the pixel brightness (amplitude) and calculates the round trip signal travel time for the range location (phase) of each pixel. A digital SAR image is a two-dimensional array of rows and columns related with the azimuth and range locations with each pixel representing a portion of the earth surface. Within each pixel there is a complex number that contains amplitude and phase information of the microwave signal reflected back by the scatterers such as buildings, vegetation, rocks, etc. The amplitude indicates strength of the reflected signal the phase shows the position of a point in time on a waveform cycle (Podest, 2017). The magnitude of the amplitude (brightness) is related to the characteristics of the scatterers on the surface, which the urban areas and rocks usually reflect back the signal better, while some smooth surfaces like water basins do not reflect back the signal to the sensor very well. In the following figure, a Sentinel-1 intensity image of Mazari Sharif in Afghanistan is shown which the size is around 20.5 Km in azimuth and 28.1 Km in the range direction with the date of acquisition 2018.11.12 in the descending mode. As seen in the figure, most of the bright areas indicate the city of Mazari Sharif as the buildings and infrastructures are good backscatterers. On the other hand, some of the agricultural land around the city are having less intensity together with parts of the mountainous areas in the Southwest due to the effects of shadow and layover.

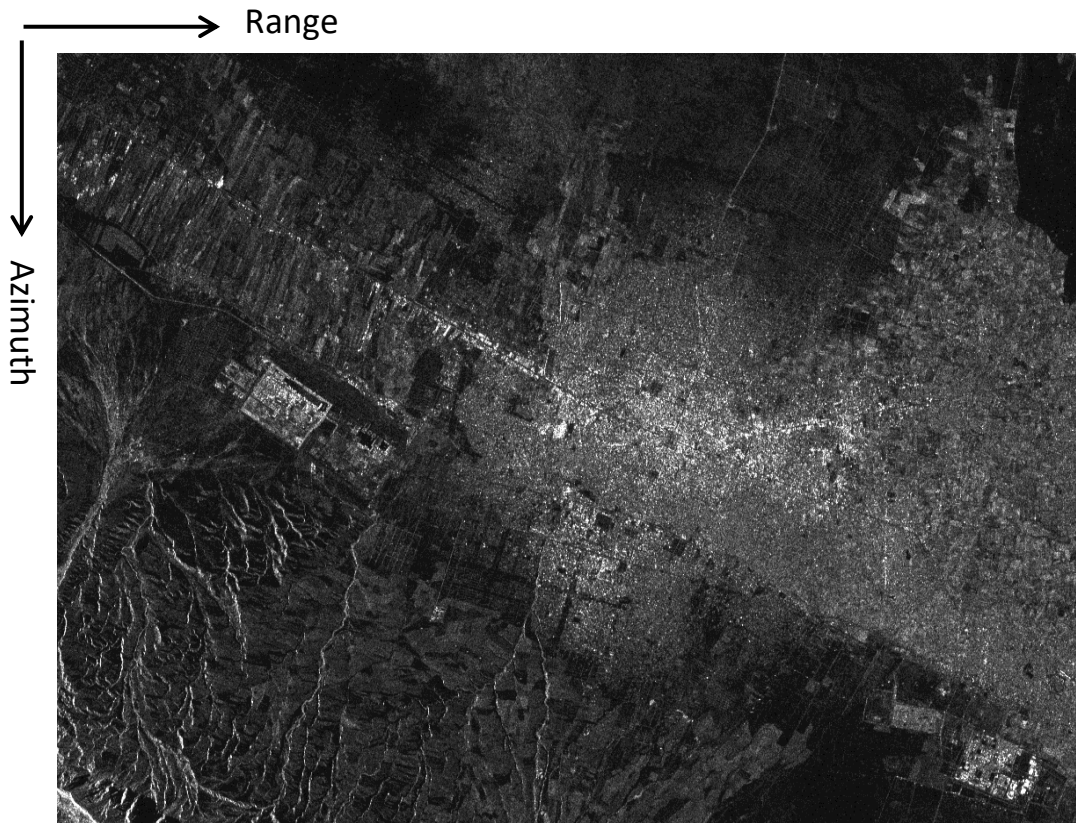


Figure 2-4: Sentinel-1 Intensity Image of Mazari Sharif (Afghanistan).

2.2 SAR Interferometry

2.2.1 Introduction

The SAR satellite acquires radar images over the same area in different time steps. With the availability of data over an area in different times, the SAR Interferometry could be generated. The idea of SAR Interferometry is to derive information about an area considering the phase information of at least two complex-valued SAR images. Therefore, by cross-multiplication of the pixel by pixel of the first SAR image with the second one, the SAR Interferogram is produced (Bamler & Hartl, 1998). In this process, the Interferogram amplitude will be the amplitude of the first image multiplied by the amplitude of the second image, and the Interferogram phase will be the phase difference between the two images. The following figure by (Bamler & Hartl, 1998) shows the SAR Interferometry concept by an example from “across-track interferometry” which is a model for reconstruction of the Earth topography using two SAR antennas operating simultaneously known as “single-pass interferometry”.

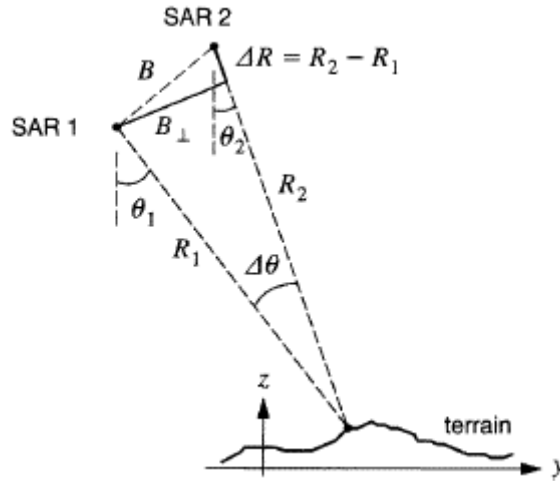


Figure 2-5: Across-track interferometry to explain the phase difference. Source: (Bamler & Hartl, 1998)

The phase of the first and second SAR images are shown respectively as below:

$$\varphi_1 = -2kR_1 + \varphi_{scatt,1} \quad (2)$$

$$\varphi_2 = -2kR_2 + \varphi_{scatt,2} \quad (3)$$

Where R_1 is the distance (range) from the first sensor to the target and R_2 is the distance from the second sensor to the target and φ_{scatt} is generated due to the phase shift by the scatterer. Considering that both images have the same scattering phase, the phase difference is calculated as below:

$$\varphi = \varphi_2 - \varphi_1 = 2k(R_2 - R_1) = \frac{4\pi}{\lambda} \Delta R \quad (4)$$

In the above formula, λ is the radar wavelength, 4π factor is due to the two way path from the sensor to the target and back to the sensor. In the case of landslide studying, considering the fact that the target moves to a new position in the second acquired SAR image due to the displacement, the phase difference equation could be further expanded as DInSAR observation equation (Crosetto, Monserrat, Cuevas-González, Devanthery, & Crippa, 2016).

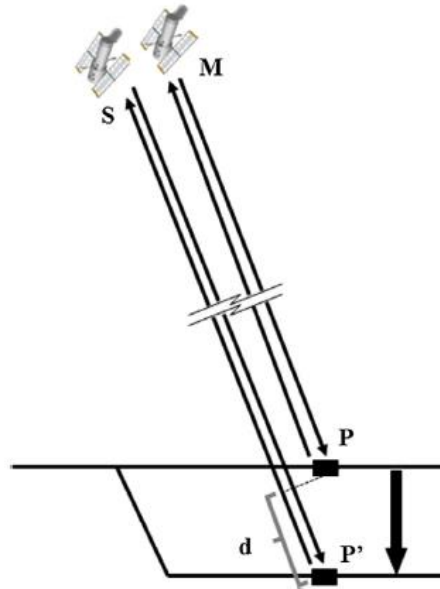


Figure 2-6: Deformation “d” between two SAR image acquisition. Source: (Crosetto et al., 2016)

$$\Delta\varphi = \varphi_{disp} + \varphi_{topo_res} + \varphi_{atm} + \varphi_{orbit} + \varphi_{noise} \quad (5)$$

Where the φ_{disp} is the phase component due to displacement in the line-of-sight (LOS), φ_{topo_res} is residual topographic error phase component after removal of topographic phase component by a Digital Elevation Model (DEM), φ_{atm} atmospheric phase component due to the changes in the atmospheric condition of two acquisitions, φ_{orbit} the orbital errors phase component which is due to the error for the position of the satellite in the orbit and φ_{noise} basically as the noise phase component. (The most important goal in this thesis is to derive the φ_{disp} from the DInSAR).

2.2.2 SAR Interferometric Process

The SAR Interferometric Process starts with having a data of master and slave images. Using a Digital Elevation Model (DEM) the Interferogram product could be generated. In the below figure, a detailed process of Repeat-pass Interferometric process which means the images are acquired over different times is explained.

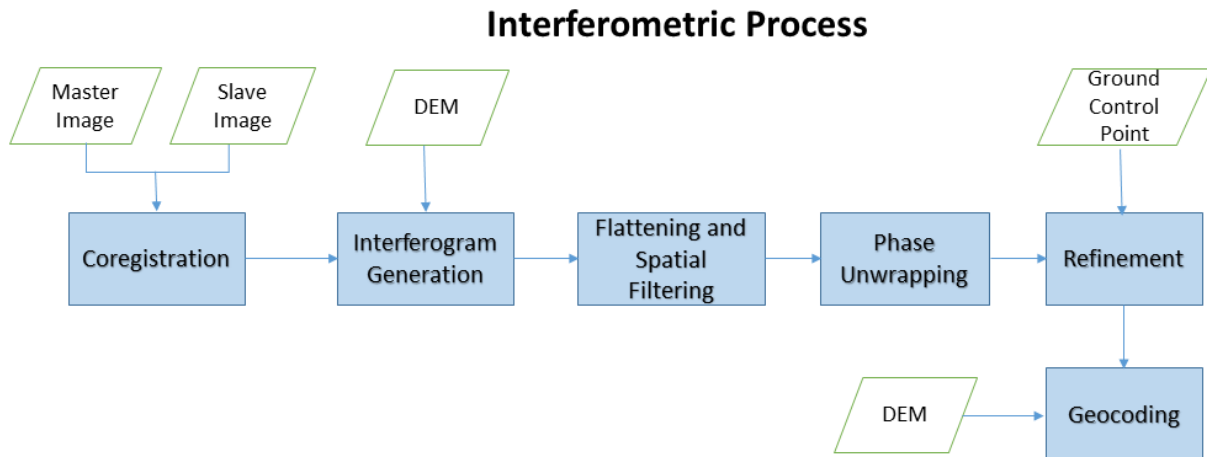


Figure 2-7: Interferometric process of SAR Images

2.2.2.1 Coregistration

In the first step, the master and slave images need to be coregistered on each other. Because the images are acquired at different time and the satellite position at each acquisition time might not be the same and there is a change in azimuth and range position of pixels for each point on the ground. Therefore, the amplitude cross-correlation with a search window is carried out to find the shift in azimuth and range direction of the master and slave image. In order to explain the Interferometric Process, an Interferogram is generated on the landslide in North of Iran. The date of the landslide occurrence is 25.10.2018 and the following multi-looked master (15.10.2018) and slave (20.11.2018) images are acquired before and after the landslide occurrence date in order to observe the changes on the ground surface respectively. The following multi-looked master and slave intensity images are downloaded from Sentinel-1 ascending mode.

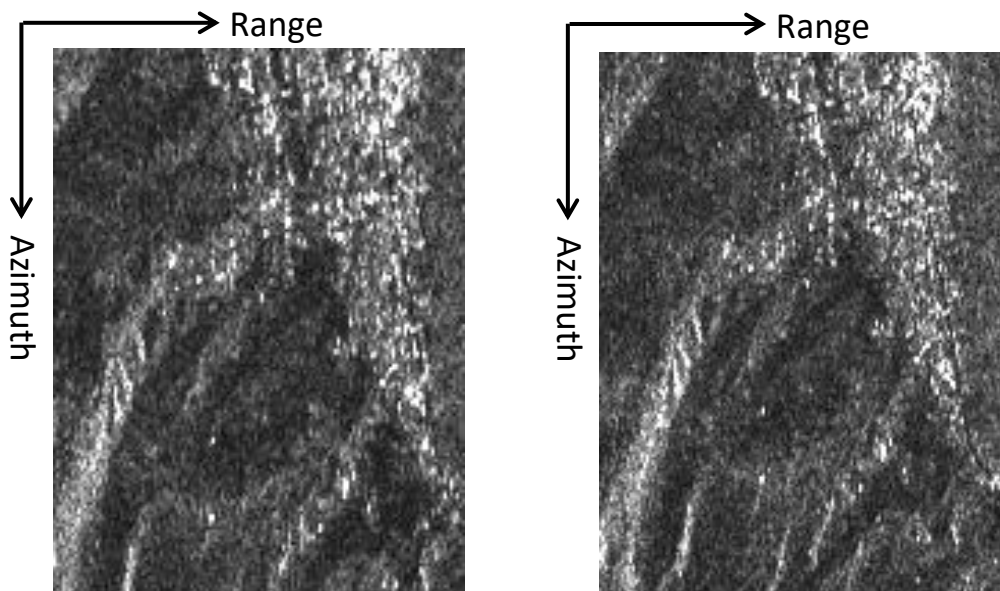


Figure 2-8: The left figure is the Master Intensity Image and the right figure is the Slave Intensity Image from Sentinel-1.

2.2.2.2 Interferogram Generation

In the next step, the Interferogram product is generated by the phase difference between the two coregistered SAR images. The interferometric phase is calculated based on the imaginary part as $Imag(I)$ and real part as $Real(I)$ of the interferogram (SARscape User Guide, 2014).

$$phase = \text{atan} \left(\frac{Imag(I)}{Real(I)} \right) \quad (6)$$

As a result the interferogram is formed which is shown below together with the digital elevation model (DEM) of SRTM-1 with a 30 x 30 meters spatial resolution corresponding to the study area.

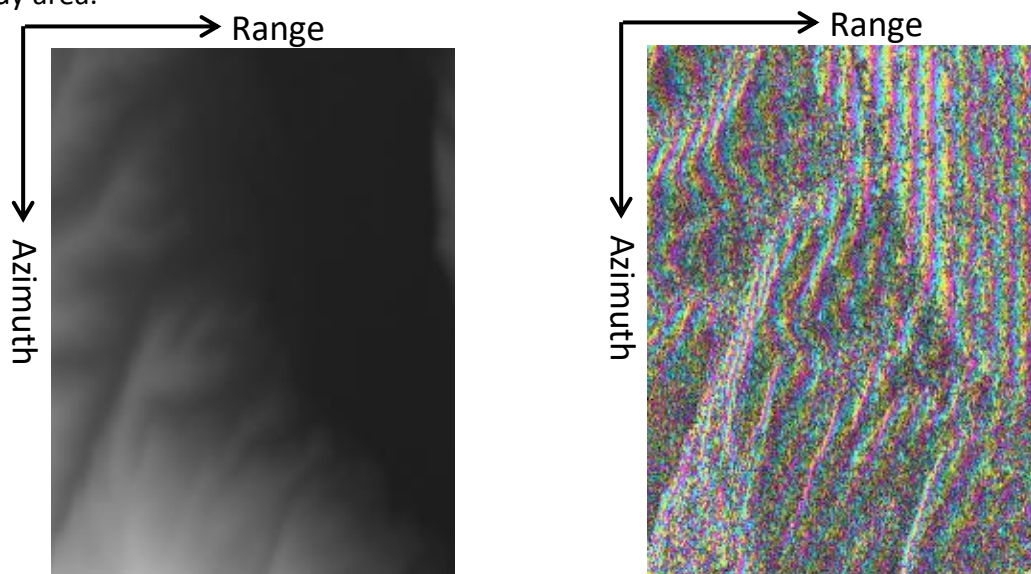


Figure 2-9: The left figure is a SRTM-1 Digital Elevation Model and the right figure shows the initial interferogram product.

The spectral shift and Doppler bandwidth filtering are applied in the interferogram product. The spectral shift helps to manage the range spectra shift caused by the different SAR viewing angle on the ground targets. On the other side, the Doppler bandwidth filtering compensates for different Doppler or squint angles that bring about shifted azimuth spectra in the SAR images (SARscape User Guide, 2014).

2.2.2.3 Flattening and Spatial Filtering

In the next step, Interferogram flattening is applied using a Digital Elevation Model (DEM) shown in the figure 2-9. The accuracy of the DEM affects the topographic phase contributions, therefore, the used SRTM-1 DEM of 30 x 30 meters resolution could be the best input reference digital elevation model in this study. As a result of this process, the output is a flattened Interferogram with the constant phase due to the acquisition geometry and the topographic phase based on an input DEM are removed.

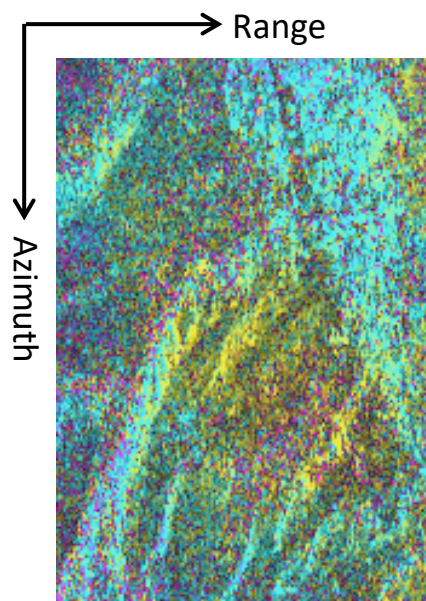


Figure 2-10: The flattened Interferogram after topographic phase removal

The interferogram needs to be filtered in order to remove some available noise and improve the interferometric fringe quality. The Goldstein filtering improves fringe visibility and reduces the noise caused by the temporal or spatial baseline decorrelation. This filtering method works based on a parameter known as “alpha” which shows the strength of the filter and is formulated in an adaptive way on the basis of the local scene coherence, as the lower the coherence the stronger the filter will function. Therefore, the incoherent areas are filtered

more than the areas with higher coherence which indicates the signal loss minimization that strongly reduces the noise level (SARscape User Guide, 2014).

The Coherence or interferometric correlation is the ration between the coherent and incoherent summation and is shown as below.

$$\gamma = \frac{|\sum s_1(x).s_2(x)^*|}{\sqrt{\sum |s_1(x)|^2 . \sum |s_2(x)|^2}} \quad (7)$$

Which the estimated coherence values are between 0 and 1 and depend on the systematic spatial decorrelation (e.g. additive noise) and the temporal decorrelation between the master and slave acquisition times. The estimated coherence product contains the following characteristics. First, it can help to determine the measurement quality such as the interferometric phase. Generally, the SAR image pairs having low coherence values should not be used to derive reliable phase measurements. Second, the coherence values expose the information regarding the ground target scatterers and their temporal changes within different acquisition times. Basically, with the bigger temporal baseline between the master and slave acquisitions, the coherence values tend to decrease more. In the following figure, the estimated coherence values for the study area is shown with the white values near to 1 and the black color represents the 0 values.

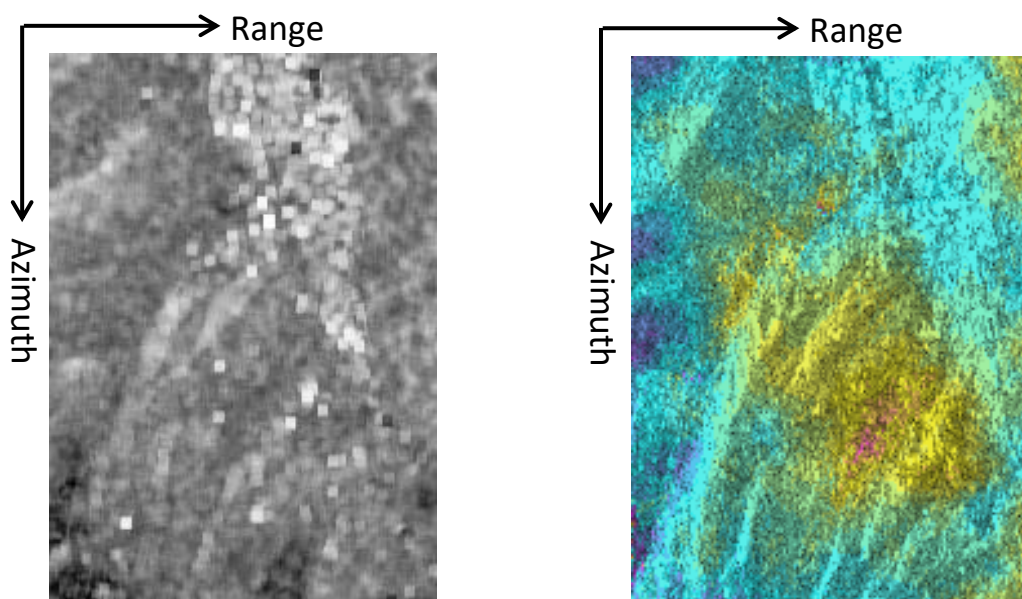


Figure 2-11: The left image shows the estimated coherence values with the black color as 0 and white color as 1 values. The image on the right represents the filtered interferogram based on Goldstein filtering method.

2.2.2.4 Phase Unwrapping

The interferogram phase is modulated between $-\pi$ and $+\pi$ (2π) which means if the phase change becomes larger than 2π , another phase begins and this process repeats on. The phase could be unwrapped by integrating the phase difference between neighboring data points in order to resolve the 2π phase ambiguity.

$$\varphi_{unwrapped} = \varphi_{wrapped} + k \cdot 2\pi \quad (8)$$

The phase ambiguity term “k” is unknown and based on that the absolute displacement cannot be determined. Hence, the phase needs to be unwrapped to determine the number of interferogram phase change cycles.

There are many phase unwrapping algorithms such as region growing, minimum cost flow, minimum least squares, multi-baseline, etc. In this study, the Minimum Cost Flow method is introduced. This method considers a square grid over all the image pixels. If the coherence value in the pixels are lower than a threshold, they are masked out and removed from the final results. Here an unwrapping coherence threshold of 0.2 is applied. In additions, it could be mentioned that there are some factors which make the phase unwrapping process difficult such as big movements or the phase noises (e.g. temporal decorrelation) and they might result to errors in the produced results.

2.2.2.5 Refinement and Reflattening

The interferogram product could be further refined by correcting the possible inaccuracies in the orbit information, calculating the phase offset for obtaining the absolute phase values or by removing possible phase ramps. Therefore, it is important to select Ground Control Point (GCP) which are points on the earth surface that are used to geo-reference the SAR images. The following images show the refined and reflattened results of the filtered interferogram and the unwrapped phase.

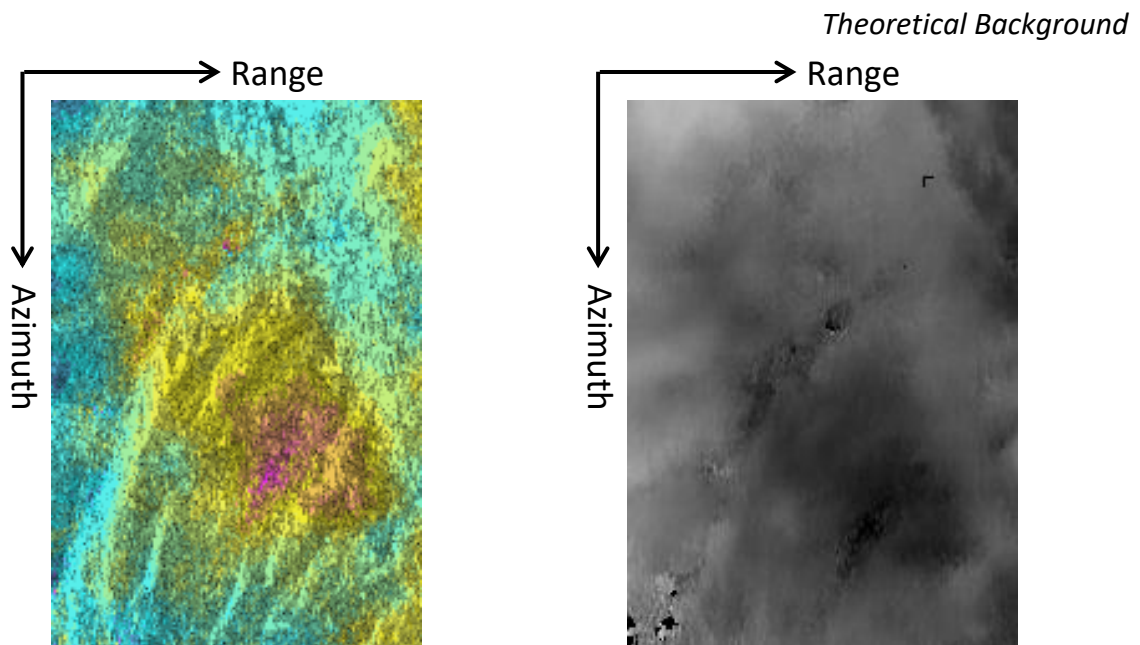


Figure 2-12: The left figure shows the refined filtered interferogram. The right figure indicates the refined unwrapped phase.

2.2.2.6 Geocoding

The InSAR measurement is in the slant range geometry (LOS) which is the line-of-sight from the sensor at the satellite platform to the target on the ground. This geometry consists of the SAR image in the range and azimuth direction that needs to be transformed into the Global Cartesian coordinate system such as WGS-84 in order to obtain the local area's geographic coordinates. The position of every pixel could be estimated in a geocoded reference frame by using the orbit parameters and the DEM.

2.3 Time Series Analysis

2.3.1 Persistent Scatterers Interferometry (PSI)

The Persistent Scatterer Interferometry (PSI) is a time series analysis method that is able to measure the temporal evolution of ground surface deformation. The most important approach is proposed by (Ferretti et al., 2001) which offers a complete solution for selecting the PS candidates, dealing with temporal and geometrical decorrelation. The deformation time series could be used for many applications such as analyzing the kinematics of different phenomena such as velocity, acceleration and activation of natural and human-made hazards like landslides, earthquakes, volcano activities, etc. The PSI idea is to have a series of SAR images and they are coregistered on a selected master image and the interferograms are created from each slave image with respect to the master image.

A minimum number of 3 SAR images are required to perform PSI algorithm, but it is suggested to include at least 20 images to obtain reliable results especially if the coherence in the study area is low.

The only drawback about this method could be the selection of scatterers with high coherence even at the large baselines which generally brings about low PS point density in the nonurban areas (Crosetto et al., 2016).

According to (Ferretti, Prati, & Rocca, 2000) the time and space analysis of PSI is performed to identify the different interferometric phase contributions to acquire a better measurement of the ground surface deformation. The PSI steps are shown in the following figure.

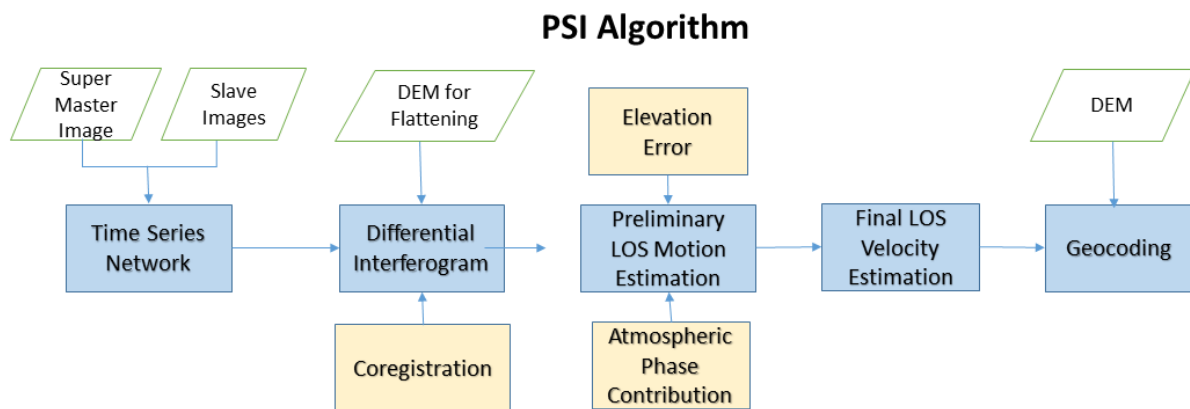


Figure 2-13: Persistent Scatterers Interferometry (PSI) algorithm steps.

At first, the time series network is created using a Super Master image which all the other slave images are coregistered onto the master acquisition. The N differential interferograms are generated from N+1 SAR images and are flattened using a DEM by removing the topographic phase component. From here, the preliminary LOS motion, elevation error and atmospheric contribution are estimated which due to the inaccuracy of the DEM, the topographic phase component may not be perfectly removed from the interferograms. In fact, the better the DEM accuracy or resolution is, the better the topographic phase component is removed. Next, the estimated values are improved by spatial smoothing of the phase residuals. The final outputs such as displacement velocities, residual height, etc. are geocoded and projected onto the DEM cartographic system.

2.3.1.1 PS Candidate Selection

The PSI method focuses on the pixels that have high coherence during the time series, and this brings about more number of observations. According to (Ferretti et al., 2001), the PS candidates are selected as the stable targets through the coherence map of the interferograms. The correlation thresholding which examines if a target has a coherence always bigger than a threshold could be an easy approach to select the PS candidates. Moreover, the bright radar scatterers have a consistent pixel phase information over a time interval. The idea (Ferretti et al., 2001) is to analyze the amplitude variation for each pixel alone in an interferogram series using an initial set of PS pixels with a high signal-to-noise ratio (SNR). Next, each pixel is tested for phase stability (Hooper, Segall, & Zebker, 2007).

The Amplitude Dispersion Index “D” measures the amplitude variation in the time interval with the Phase standard deviation (σ) measures the variation of phase respectively. The following figure shows the amplitude dispersion in the time domain.

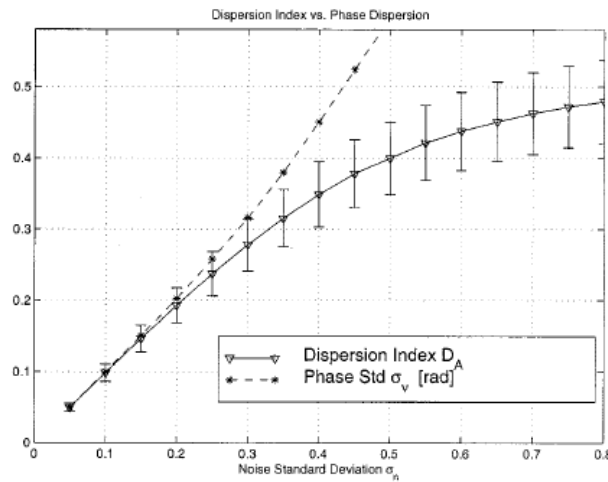


Figure 2-14: Amplitude Dispersion Index (Ferretti et al., 2001)

The amplitude dispersion index by (Ferretti et al., 2001) could be defined as below:

$$D_A = \frac{\sigma_A}{\mu_A} \quad (9)$$

Where the σ_A refers to the standard deviation and μ_A the mean for a series of amplitude values. Later a threshold is applied on D_A to select a subset of pixels. Therefore, the pixels that are consistently bright and have high coherence throughout the time series make the search for the PS candidate selection process easier.

The density of PS points ranges from low density in the vegetated and forested areas to high density in the urban areas with buildings, poles, exposed rocks, etc. In additions, there are sometimes no PS points available in the areas covered with snow and the construction works.

2.3.1.2 Line-of-Sight deformation

The PSI deformation consists of line-of-sight (LOS) measurements, which indicate the measurement in direction from the sensor to the ground target. In this case, the displacement happens either away or towards the satellite’s LOS as 1D measurement type. The 2D and 3D measurements could be derived from the LOS measurements using different methods respectively.

2.3.2 Small Baseline Subset Interferometry (SBAS)

The Small Baseline Subset Interferometry (SBAS) time series analysis method examines a proper combination of differential interferograms having small spatial (orbit separation) and temporal baseline for the goal of decreasing the spatial decorrelation phenomena. In the following figure, the steps necessary for the SBAS method is explain in a sequential graph.

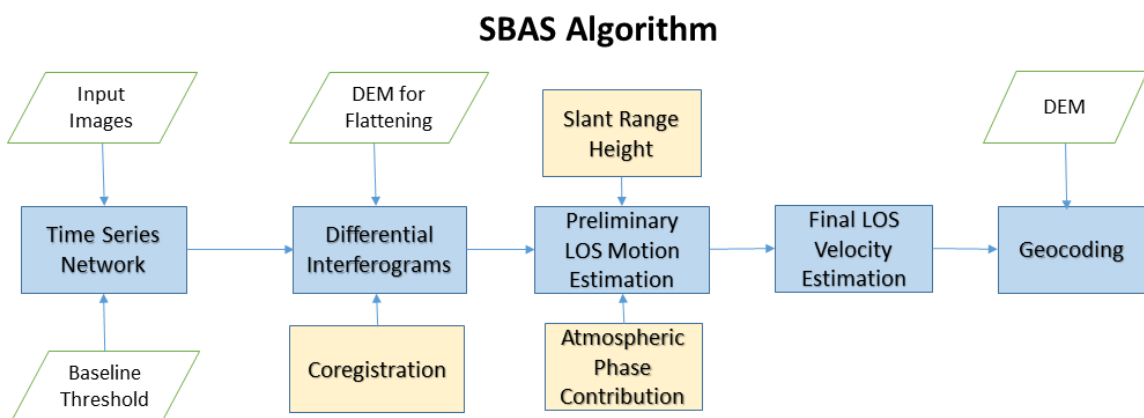


Figure 2-15: Small Baseline Subset Interferometry (SBAS) algorithm steps.

In the SBAS method compared to PSI method which uses a super master image, all the input images are connected in a network of master and slave pairs in which the interferograms are generated only based on the threshold values set for the spatial and temporal baselines.

The spatial baseline describes the distance between the sensor positions at different acquisitions in the orbit and the temporal baseline indicates the time difference between the acquisitions respectively. Later the interferograms are generated between the connected pairs and they are flattened and filtered, and the unwrapped phases are produced. The interferogram flattening is done using the input DEM. The related displacement products such as date by date value, velocity and acceleration and height (new slant-range DEM) are created. The atmospheric corrections due to the spatial and temporal variations are also performed. At the final step, the results are projected onto the cartographic system.

3 Methodology

In this thesis the goal has been to focus on the kinematics of the slow moving landslides to examine their behavior and characteristics. In order to achieve this aim, the time series analysis method are useful to study the slow moving landslides over a desired time interval. Nowadays with the availability of SAR data from different satellite missions, such studies have become easier to be performed. Hence, within the scope of this thesis, the two time series analysis methods of Persistent Scatterer Interferometry (PSI) and Small Baseline Subset (SBAS) are applied. From both methods the average displacement velocity are obtained in the line-of-sight (LOS) direction in the unit of “mm/year”. The 1D LOS displacement velocity values are in two ranges:

- Positive values represent the motion towards the satellite’s LOS direction.
- Negative values represent the motion away from the satellite’s LOS direction.

The post-processing of the average displacement velocity in LOS direction, follows the goal of projecting these values into the slope direction to represent the true ground surface motion in the study area. In the following figure, the methodology for the post-processing of the time series analysis outputs is shown.

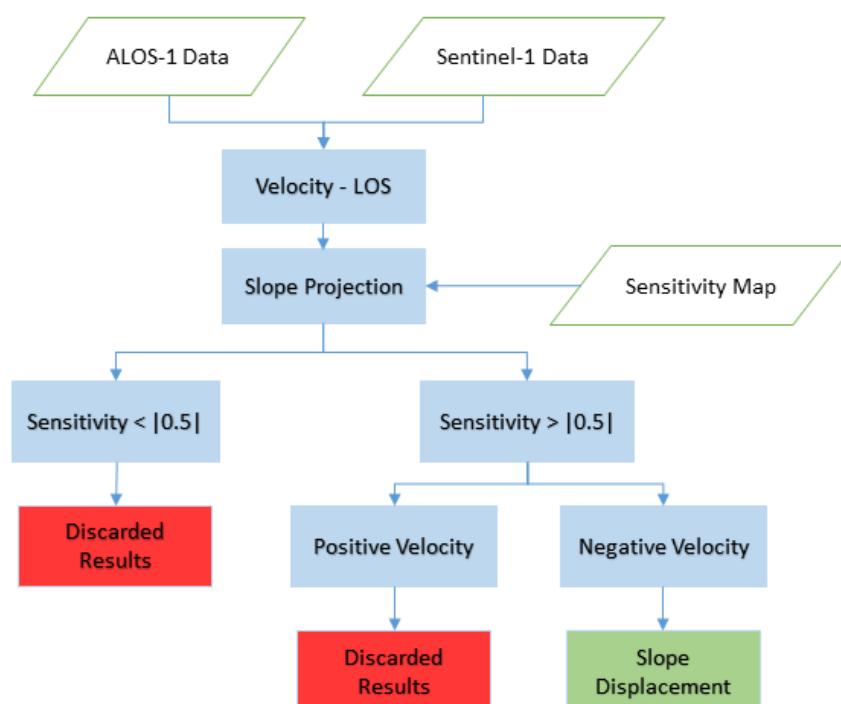


Figure 3-1: Methodology flowchart for post-processing of the LOS displacement velocity results.

The post-processing methodology considers the local topography and the satellite's acquisition geometry as the parameters to project the LOS results into the slope direction. As landslide movements are driven by the gravity, it is assumed that the displacements takes place in the slope direction. Therefore, the sensitivity of the InSAR LOS measurements to the slope movement could be analyzed using the following formula (Haghshenas Haghghi & Motagh, 2016):

$$s = [\sin(u) \quad -\cos(u)\cos(v) \quad -\cos(u)\sin(v)] \begin{bmatrix} \cos(\theta) \\ \sin(\alpha) \sin(\theta) \\ -\cos(\alpha) \sin(\theta) \end{bmatrix} \quad (10)$$

In which “ s ” is the sensitivity of LOS measurement to the motion in the slope direction for a certain point, “ u ” the degree of slope steepness and “ v ” the aspect or orientation of the slope, θ is the incidence angle and α the heading angle of the satellite. The sensitivity values range from -1 to +1 with 0 value containing the less sensitivity. Therefore, the bigger the sensitivity's absolute value the more sensitive is a point on the ground to the InSAR LOS measurement.

In order to create the sensitivity map for the whole study area, the aspect and slope parameters for every point on the ground is calculated from a SRTM-1 DEM with 30 meters resolution which are shown respectively below.

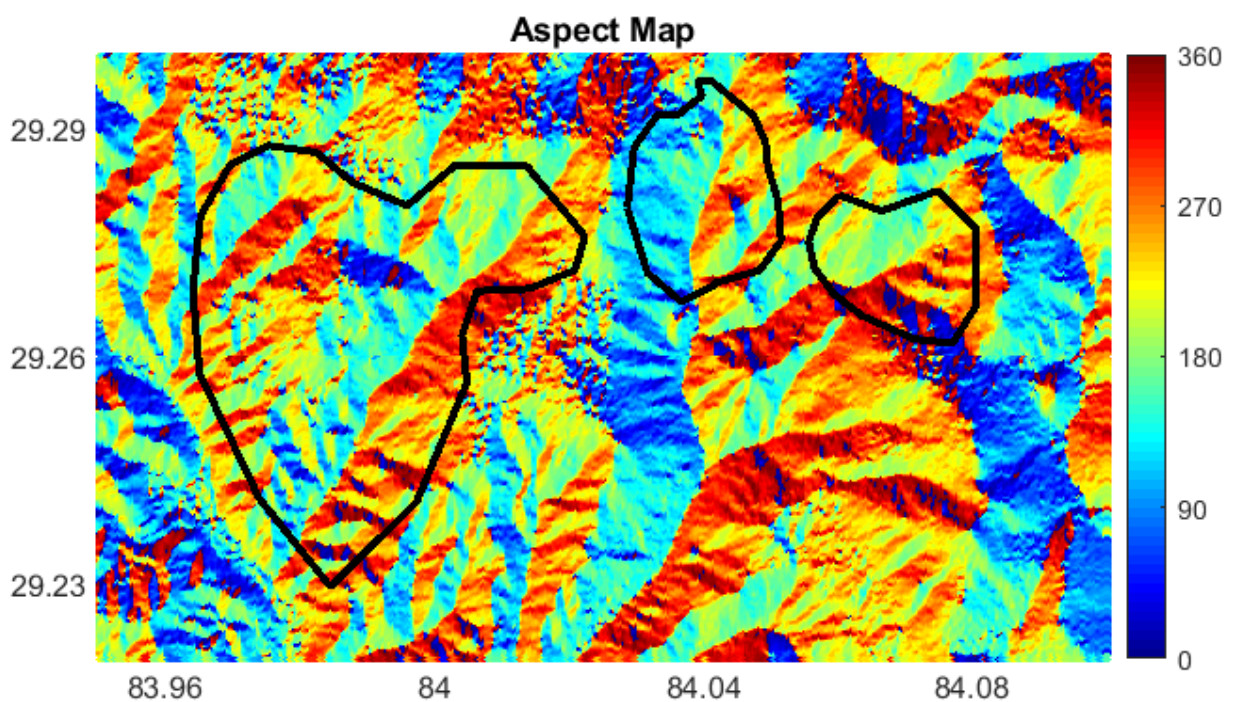


Figure 3-2: Aspect Map of the study area. The unit is “degree”.

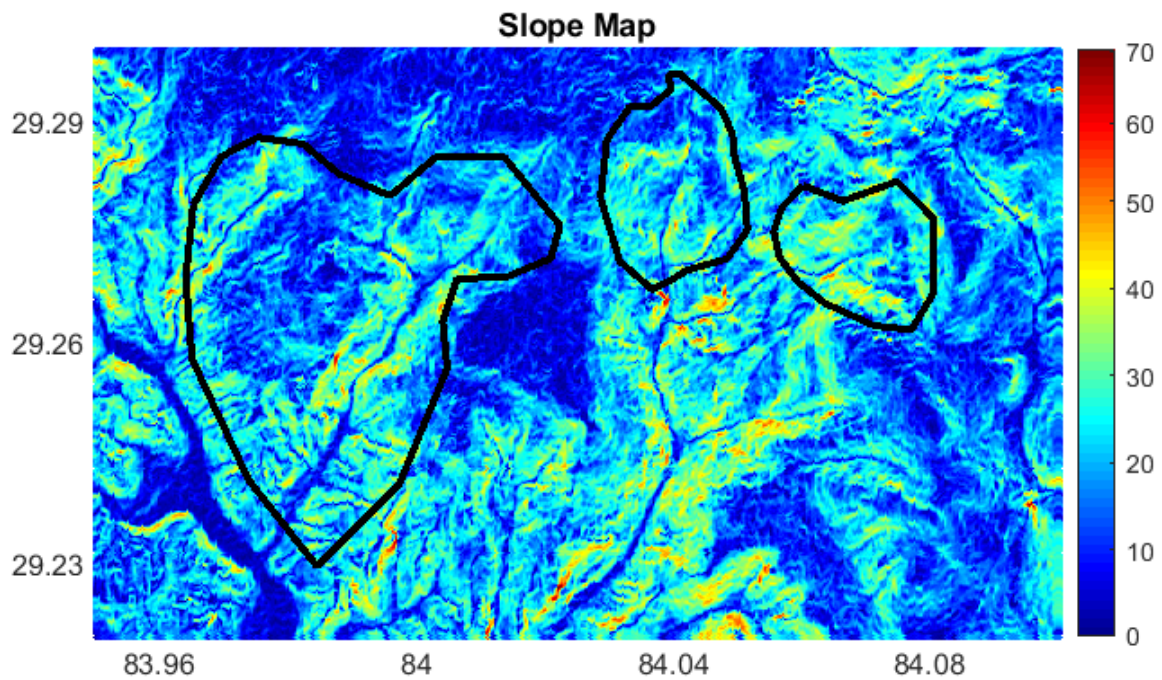


Figure 3-3: Slope Map of the study area. The unit is "degree"

The aspect map shows the slope directions which its values could be classified for instance as 0° indicating the North direction, 90° the East, 180° the South, 270° the West and similarly 360° indicating again the North direction. As seen in the above figure, the slope direction is different in each landslide area, with more Southeast and Northwest directions in the first study area, more East and West directions in the second one, and mostly North and South directions in the third area.

The slope map describes the steepness or degree of inclination of a point relative to the horizontal plane. It is expressed as an "angle" with 0° as fully horizontal and 90° as fully vertical slopes. The slope degree in the study area ranges mostly between 30 and 40 degrees.

Having the slope and aspect map derived from the reference DEM together with satellite's incidence and heading angle, the sensitivity of InSAR measurement is calculated for every point on the ground for the study area.

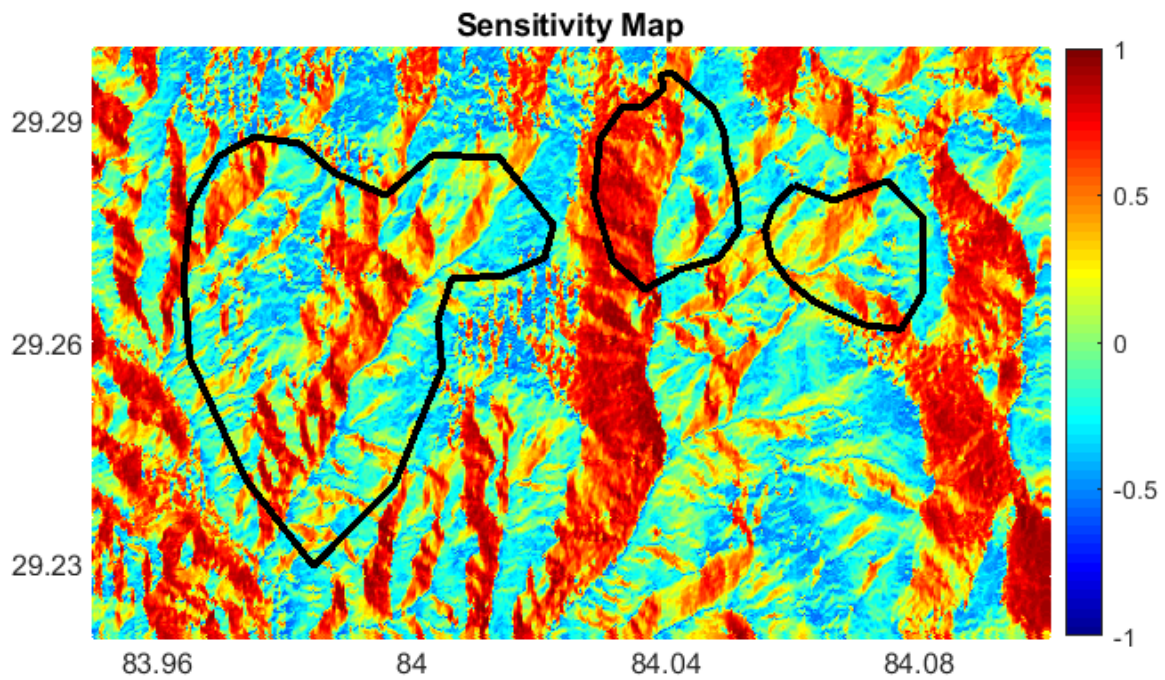


Figure 3-4: Sensitivity Map of InSAR measurement to slope displacement

The generated sensitivity map proves that the slopes mostly to the East direction are more suitable for the slope displacement with respect to the InSAR LOS measurement. This could be an advantage for the InSAR measurement to detect the real deformation in the areas with higher sensitivity, however, as the slope degree and direction varies significantly throughout the study area, it might be challenging for the areas with less sensitivity to lose information regarding the deformation phenomena.

4 Data overview

SAR data are available from variety of satellite missions. There are two types of accessing the SAR data which the first one is to obtain free data by registering through online portals such as Earth Online (<https://earth.esa.int/web/guest/home>) from the European Space Agency (ESA). The data access is granted to the user typically within one or two working days from acceptance. The other type is to request the data by a project proposal describing the aim of the scientific tasks. In this case, the notification about the view result and data access is evaluated typically within 6-8 weeks. The timeline of the SAR satellite mission is shown in the following figure.

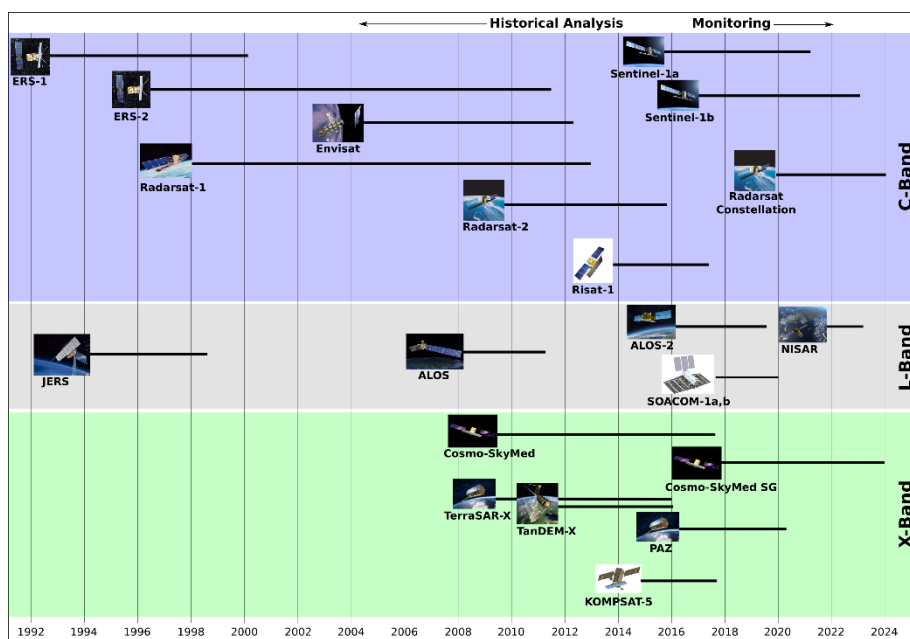


Figure 4-1: SAR Satellite Missions. (UNAVCO)

The L-band SAR data are obtained from the ALOS-1 satellite mission. The Advanced Land Observing Satellite (ALOS) was launched and operated into a sun-synchronous orbit by Japanese Aerospace Exploration Agency (JAXA) between the periods 2006 to 2011. The mission's goal was to acquire radar images for the land observation applications contributing to cartography, environmental monitoring, disaster management and resource survey (Iwata, Ishida, Osawa, & Tomi, 2003). Moreover, the data covered the whole globe with an acquisition interval of 46 days (Wempen & McCarter, 2017).

The C-band SAR data are acquired from the Sentinel-1 satellite mission. Sentinel-1 system design has been driven by the need for the continuity of ERS/Envisat mission with

improved revisit, coverage, timeliness, and reliability of service. The system has been established to provide medium resolution SAR images with an Interferometric Wide Swath (IWS) 250 km and a resolution of 20m x 5m for azimuth and range directions (Snoeijs et al., 2010). Sentinel-1A was launched on 3 April 2014 and Sentinel-1B launched on 25 April 2016 with 12 days repeat cycle for each satellite which taking advantage of both makes the SAR data available every 6 days. The objective of the mission includes land monitoring (of forests, water, soil and agriculture), emergency mapping for natural disaster events, Sea ice observations and iceberg monitoring, and climate change monitoring. The Sentinel-1 SAR images for the study area are obtained from two sources which the first one is from the European Space Agency (ESA) Earth Online hub (<https://earth.esa.int/web/guest/home>) which provides free SAR data after user registration.

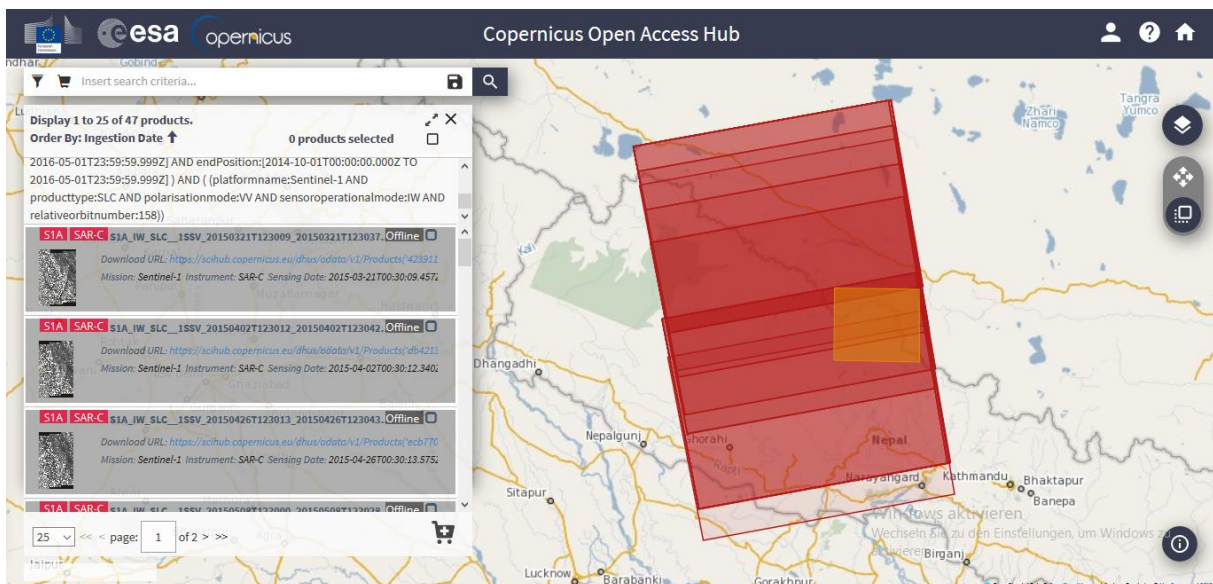


Figure 4-2: ESA Earth Online access hub for downloading Sentinel-1 SAR data.

The Alaska Satellite Facility (ASF) is a data processing facility and satellite-tracking ground station in the Geophysical Institute at the University of Alaska Fairbanks which provides free Sentinel-1 SAR data to the scientific users. Sentinel-1 SAR images are also downloaded via this online platform (<https://vertex.daac.asf.alaska.edu/>) after registration.

Figure 4-3: Vertex portal of Alaska Satellite Facility to download Sentinel-1 SAR dat

The data used in this thesis consists of L-band ALOS-1 and C-band Sentinel-1 images. As total number of images in both datasets is around 20, time series analysis methods could be implemented on them to study the kinematics of slow moving landslides. The characteristics of the data is shown in the following table and the implementation is discussed in the next chapter.

	ALOS-1	Sentinel-1
No. of Images	18	21
Pass Direction	Ascending	Ascending
Acquisition Date	2007-2011	2014-2016
Revisit time	46 days	12 days
Incidence angle	38.45°	44.5°
Frequency band	L-band	C-band
Wavelength (cm)	23.6	5.6
Spatial resolution(m)	10	20
altitude	692 km	693 km

Table 4-1: SAR data characteristics

4.1 SAR Data Processing Software and Programming Languages

The processing of SAR data has been mainly performed using the ENVI SARscape. This software is integrated with ENVI (the premier image processing and analysis solution) and has enabled the industries across the world to take advantage of available SAR data for their applications such as generating DEM products or surface deformation maps. One of the modules of this software is the “Interferometry Module” which can be used to analyze the phase information of SAR data. This module enables the users to process Interferometric SAR and Differential Interferometric SAR data for the goals of structural engineering, land subsidence monitoring, earthquakes, landslides, etc. The other module which is used mainly in this thesis is the “Interferometric Stacking Module” which integrates point-based (PSI) and area-based (SBAS) techniques for processing interferometric stacks. This module helps obtaining accurate results on both point and distributed targets (<https://www.harrisgeospatial.com/Software-Technology/ENVI-SARscape>).

The map designs has been done using QGIS software. QGIS is an open source software first created in 2002, and the developers have tried to make GIS software which is traditionally expensive commercial software, an easily accessible processing tool for everybody. This software allows the user to create, edit, visualize and analyze geospatial data. It supports both raster and vector data formats, and is integrated with shapefiles, PostGIS, web services, etc. (<https://qgis.org/de/site/>), (<https://github.com/qgis/QGIS>).

The data post-processing has been implemented using the Matlab software. Matlab makes the iterative analysis and design processes with a programming language expressed with matrix and array mathematics. Nowadays many engineers and scientists use Matlab to analyze and design their systems and products. The matrix-based Matlab language is a way to perform computational mathematics. The most important applications of Matlab are in Deep Learning, Computer Vision, Signal Processing, Quantitative Finance and Risk Management, Robotics and Control Systems (<https://www.mathworks.com/products/matlab.html>).

5 Implementation

5.1 ALOS-1 Persistent Scatterers Interferometry

The Persistent Scatter Interferometry (PSI) method time series analysis method aims to monitor the temporal evolution of the surface deformation with a measurement accuracy of few millimeters. The process starts with applying PS technique. At first, the Single Look Complex (SLC) files need to be created from the raw SAR data level 0. In the following figure, the multi-looked intensity image with multi-looking factor of 3 in range and 7 in azimuth direction are shown.

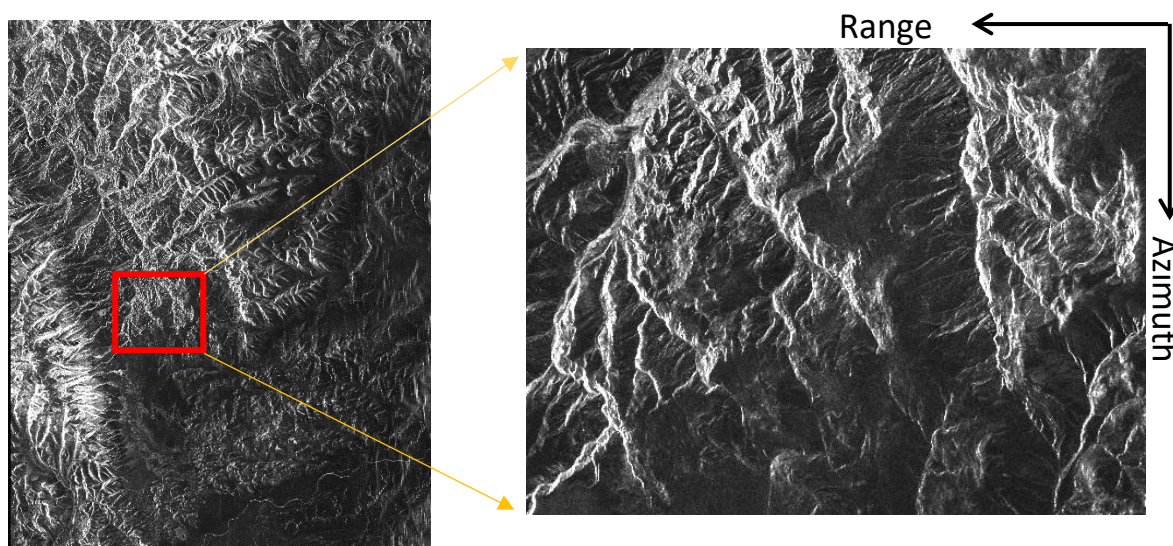


Figure 5-1: Intensity Image of the ALOS-1 data. The figure on the left is the original data. The figure on the right is the resampled subset covering the study area.

Since the data covers a large region and all of them may not be needed for the landslide analysis, parts of the data covering the study area are selected. There are 18 ALOS-1 data sets used in the PS time series analysis which their sequential number and respective acquisition dates and baseline values are shown below. The perpendicular baseline is calculated with respect to the master image which is acquired on 23.01.2009 date.

Number of Images	Acquisition Date (day/month/year)	Perpendicular Baseline (meters)
1	18.01.2007	-665
2	05.03.2007	1189

3	21.07.2007	1737
4	05.09.2007	1914
5	21.10.2007	2079
6	21.01.2008	2559
7	22.04.2008	3543
8	07.06.2008	3489
9	23.07.2008	847
10	23.01.2009	0
11	10.03.2009	385
12	26.07.2009	501
13	10.09.2009	929
14	26.10.2009	1175
15	26.01.2010	1851
16	13.03.2010	2310
17	13.09.2010	2556
18	29.01.2011	3572

Table 5-1: ALOS-1 data used in the time series analysis. The perpendicular baseline is calculated w.r.t. the master image.

In the next step, the selected input images are used to create a time series network. This step creates a SAR pair combination of master and slaves with a connection network, which will be used to generate differential interferograms respectively. In the connection network, the spatial baseline threshold could be used to select those pairs with lower than a certain spatial baseline and discard the ones exceeding the threshold value from PS analysis. The PSI time series consists of 18 datasets from 18.01.2007 to 29.01.2011 with the master image chosen in the middle of the time series on 23.01.2009 in order to decrease the temporal decorrelation. The time-position figure below represents the connection network with the normal distance from the master image on the y-axis and the input acquisition dates on the x-axis.

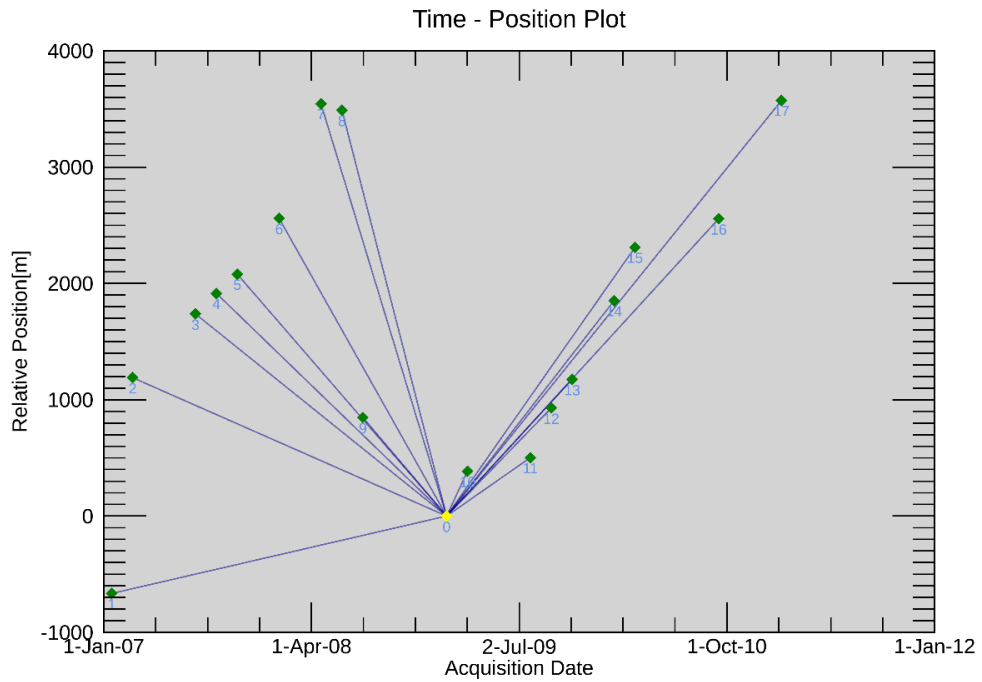


Figure 5-2: PSI time series network of slave images w.r.t. the master image shown with yellow point.

All of the images are coregistered on the master image known as Super Master image. The interferograms are generated for each slave with the same master image throughout the network. The interferograms are respectively flattened using an input reference DEM. In the following figure, the SAR intensity average image is represented which is produced from the average backscattered signals of all images in the time series network.

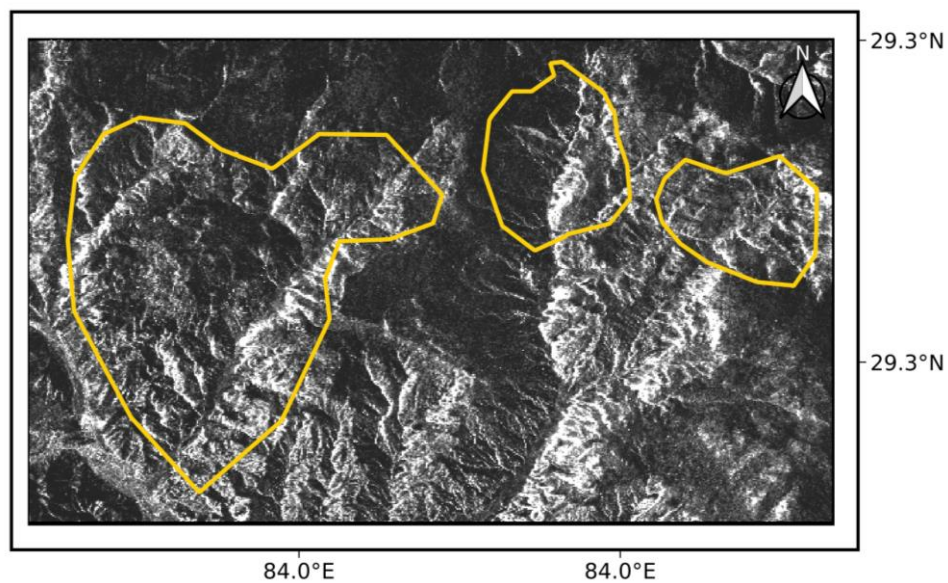


Figure 5-3: ALOS-1 SAR intensity average image

The average intensity image shows that there are many constrains such as foreshortening, layover and shadow effects due to the local topography of the study area. As

the slope changes frequently throughout the study area, different backscattered are observed as well. In some parts it may lead to the loss of coherence and from the other side, it will be challenging for the PS analysis to detect stable points as candidates in the time series.

The interferograms are created with respect to the super master image. Due to the temporal distance between the pairs, those pairs whose acquisition dates are closer to the super master date show better interferogram quality. In fact, as long as the temporal baseline value becomes, the less the quality of the interferograms becomes. This would be due to the changes on the ground surface that decreases the coherence between each acquisition.

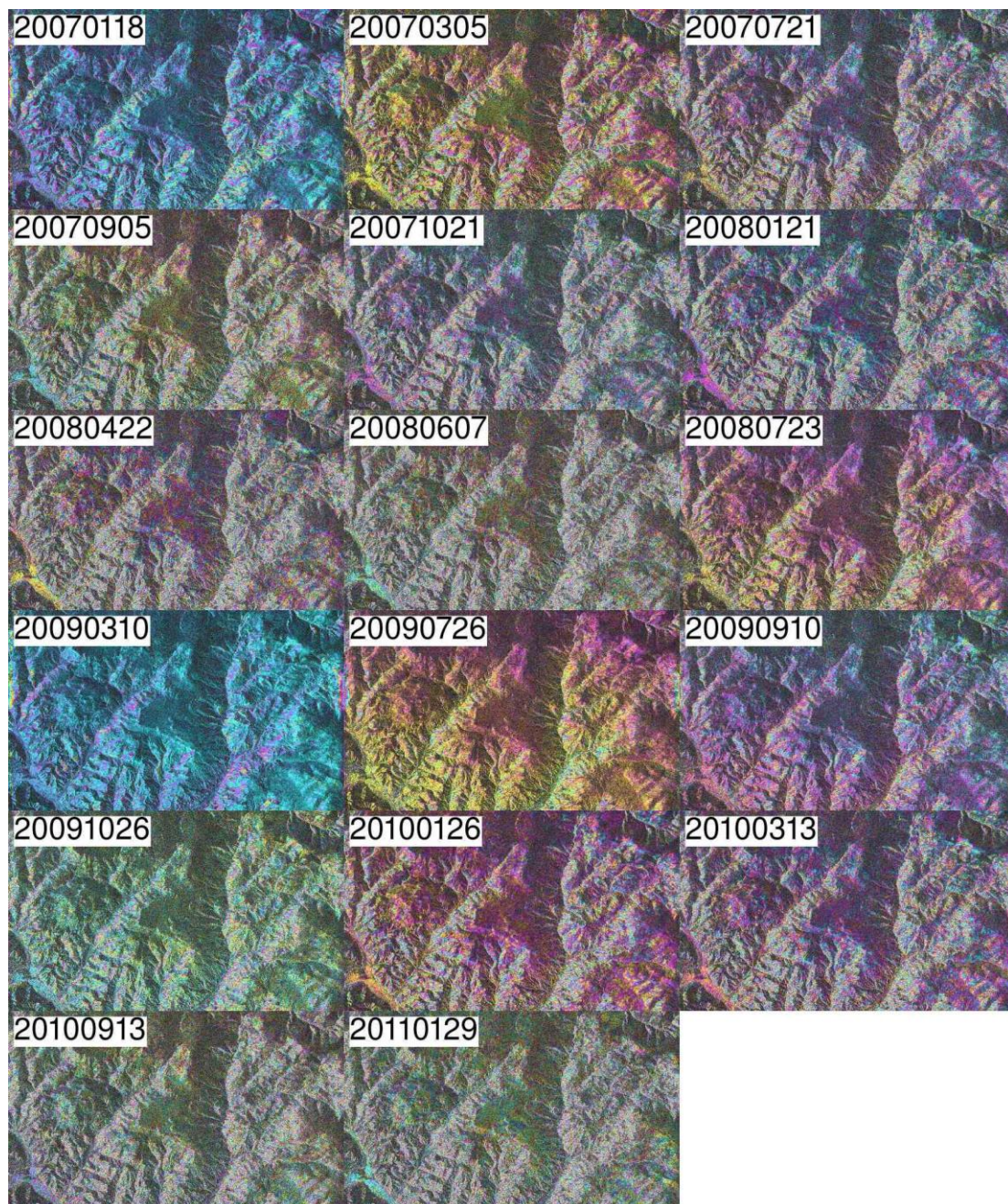


Figure 5-4: The generated interferograms for ALOS-1 data w.r.t. the super master image (01.23.2009)

In the next step, the preliminary displacement velocity and residual height products are derived. These are implemented based on the identification of a certain number of Persistent Scatterers (PS) points which are coherent radar signal reflectors. Such reliable targets are mostly found in the urban areas like roofs, poles, etc. but also the well exposed rocks could be good PS candidates. The PS technique takes advantage of the dense distribution of scatterers similar to a differential GPS technique, to remove most of the signal propagation delay caused mostly by tropospheric variations (SARscape User Guide, 2014). The multi-temporal coherence which shows how much the displacement trend fits with the PS technique model. As shown in the below figure, the bright color indicates perfect PS model match and the black color represents low or almost no model match in the study area.

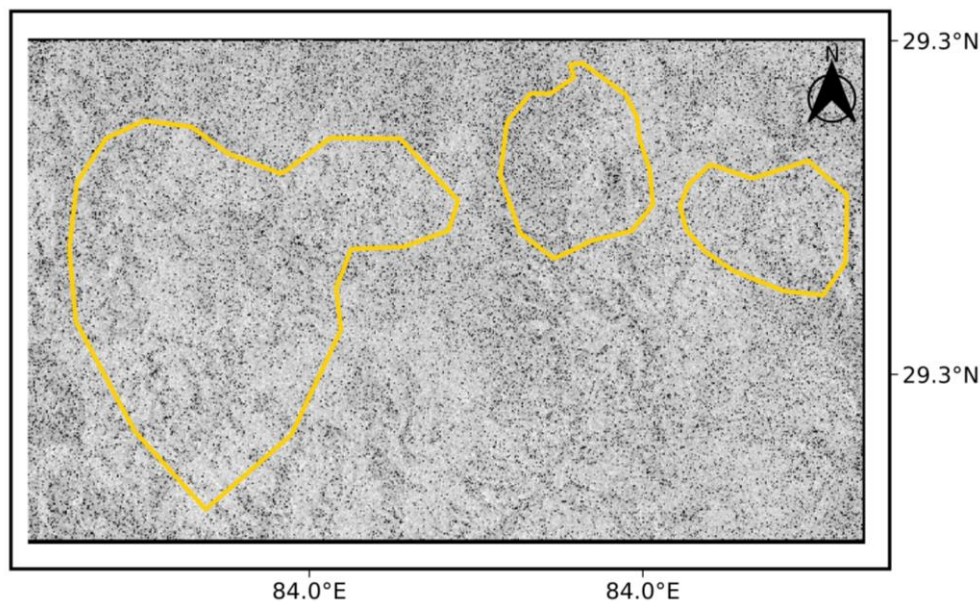


Figure 5-5: Multi-temporal coherence with white color indicating perfect PS model fit.

The atmospheric corrections on the preliminary estimated displacement velocity product is implemented in ENVI SARscape software by two filtering steps:

- **Low Pass Atmosphere:** This step corrects the spatial distribution of atmospheric effects using a square window. The larger the filter windows, the more suitable to correct the large scale effects of atmosphere. The smaller window size has a stronger filter effect and is good to correct the localized and isolated variations.
- **High Pass Atmosphere:** This step corrects the temporal distribution of the atmospheric effects again using a square window. The window size properties follows the same rules as the one in the low pass atmosphere filter.

The average displacement velocity values are derived which have the following characteristics:

- **Positive Values:** These values show the displacement towards the satellite's Line-of-Sight (LOS) which means the slant range distance from the sensor to the target has been decreased.
- **Negative Values:** These values show the displacement away from the satellite's LOS which indicate the slant range distance from the sensor to the target has been increased.

The derived average LOS displacement velocity maps for each of the three landslides are shown in the following figures. The pink point outside the landslide boundary points out the chosen reference point at which there has been no deformation. The reference point value has been subtracted from all the points inside the landslide boundary to convert the displacement results from an InSAR relative-based to an absolute estimated displacement values.

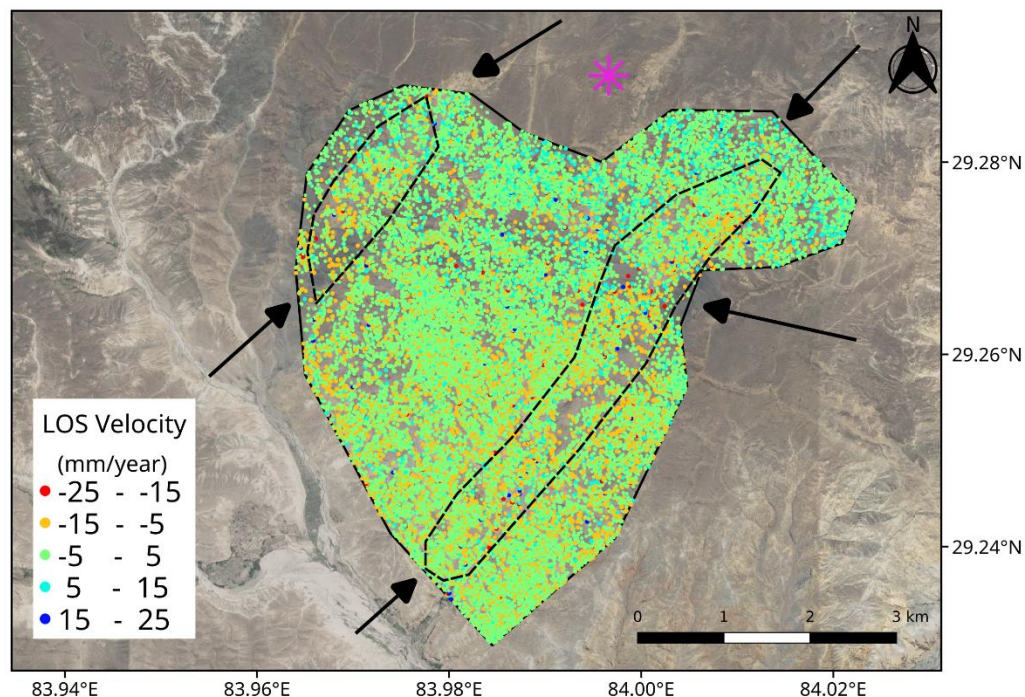


Figure 5-6: PSI average LOS displacement velocity map for the first landslide area. The unit is in mm/year.

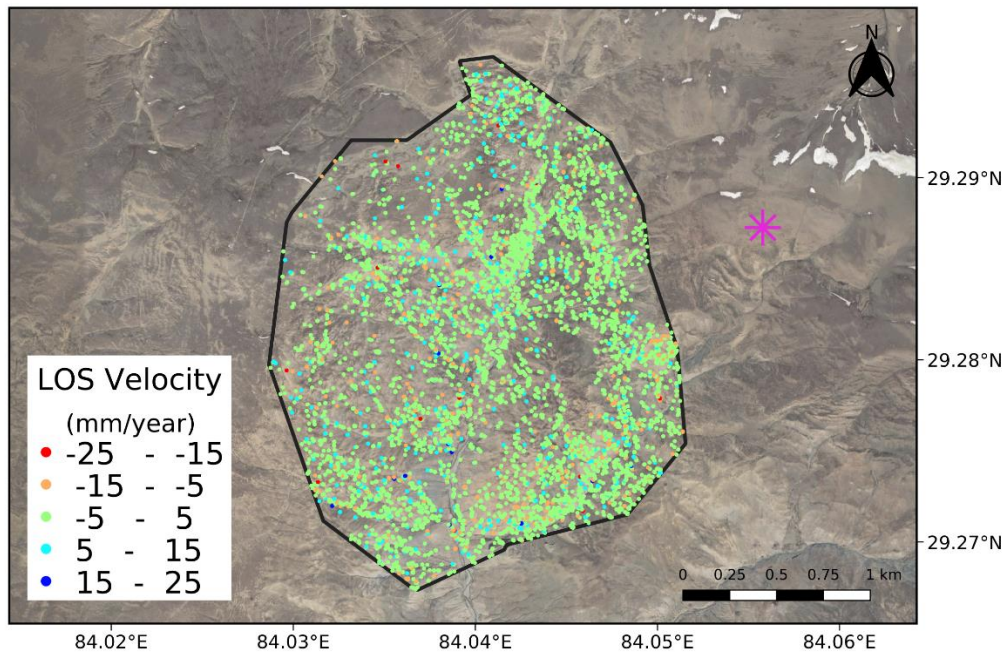


Figure 5-7: PSI average LOS displacement velocity map for the second landslide area. The unit is in mm/year.

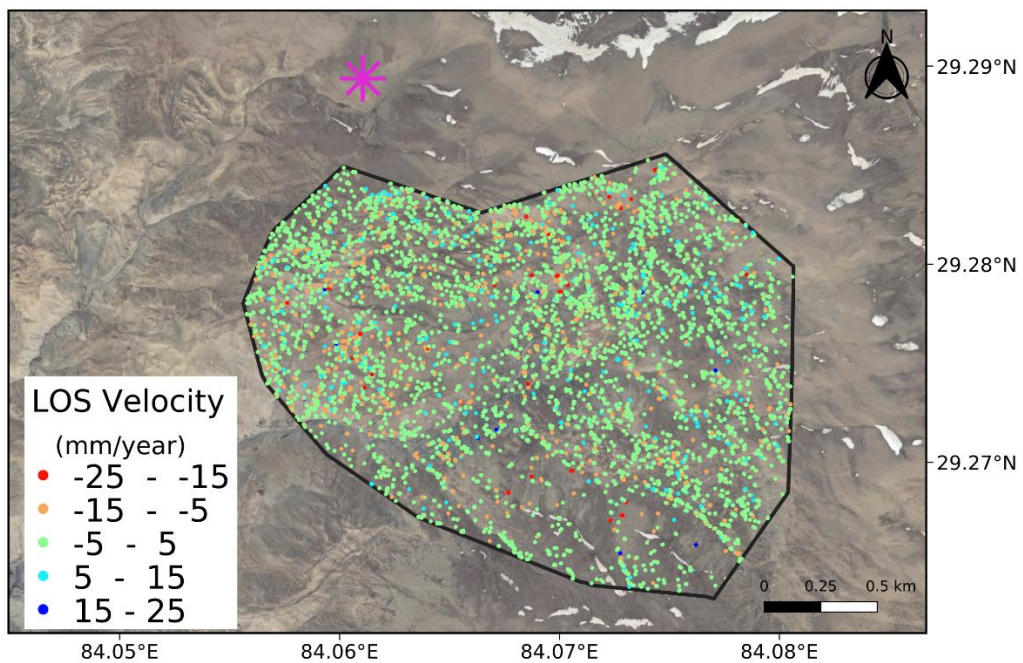


Figure 5-8: PSI average LOS displacement velocity map for the first landslide area. The unit is in mm/year.

5.2 Sentinel-1 Persistent Scatterer Interferometry

The Persistent Scatter Interferometry (PSI) time series analysis method has been applied on the Sentinel-1 SAR data acquired between 2014 and 2016 years. The Single Look Complex (SLC) files have been created from the raw SAR data level 0. In the following figure, the multi-

looked intensity image with multi-looking factor of 7 in range and 1 in azimuth direction is shown.

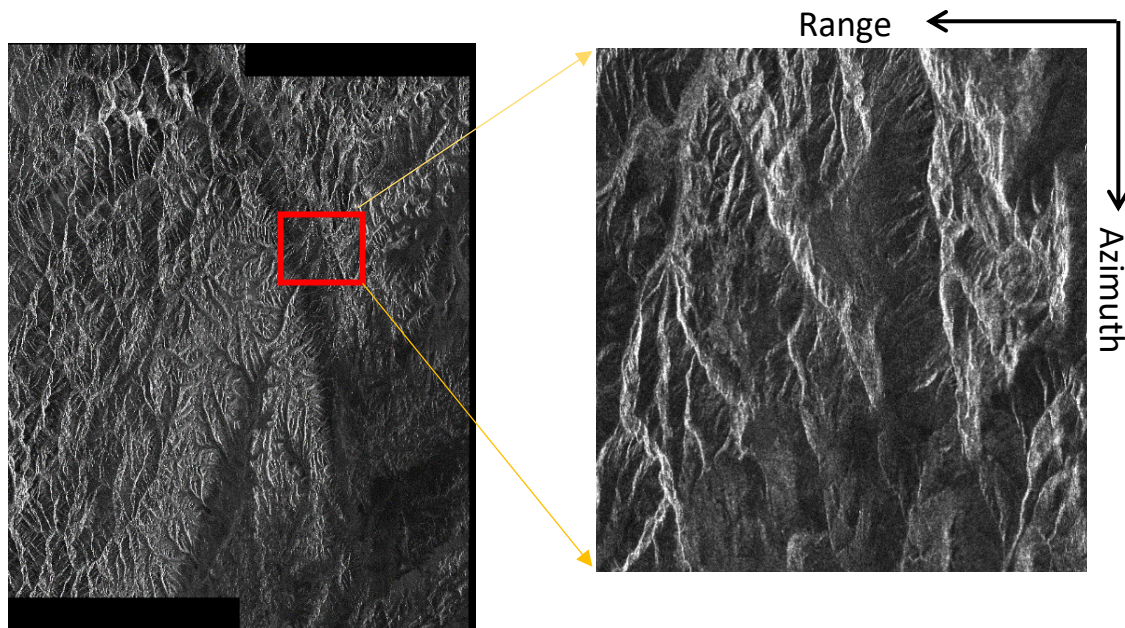


Figure 5-9: Intensity Image of the Sentinel-1 data. The figure on the left is the original data. The figure on the right is the resampled subset covering the study area.

Again similar to the ALOS-1 data, the Sentinel-1 SAR images cover a large region approximately around 250 km and therefore, parts of the data covering the study area are resampled for the landslide analysis. In the PS time series analysis 21 Sentinel-1 data sets are used which their characteristics are explained in the following table. The master image is selected on 21.03.2015 from which the perpendicular baseline value is calculated respectively for each acquisition date.

Number of Images	Acquisition Date (day/month/year)	Perpendicular Baseline (meters)
1	28.10.2014	-27
2	09.11.2014	-37
3	21.11.2014	-13
4	03.12.2014	27
5	13.02.2015	90
6	25.02. 2015	54
7	21.03. 2015	0
8	26.04. 2015	-29

9	08.05. 2015	-32
10	20.05. 2015	27
11	01.06. 2015	-47
12	25.06. 2015	-90
13	07.07. 2015	32
14	19.07. 2015	-14
15	11.10. 2015	19
16	04.11. 2015	-31
17	28.11. 2015	13
18	22.12. 2015	67
19	15.01.2016	22
20	27.03.2016	-51
21	20.04.2016	16

Table 5-2: Sentinel-1 data used in the time series analysis. The perpendicular baseline is calculated w.r.t. the master image.

The resampled images are used to create a time series network by creating a SAR pair combination of master and slaves which will be used to generate differential interferograms respectively. The PSI time series consists of 21 datasets from 28.10.2014 to 20.04.2016 with the master image chosen in the middle of the time series on 21.03.2015 in order to decrease the temporal decorrelation. The time-position figure below represents the connection network with the normal distance from the master image on the y-axis and the input acquisition dates on the x-axis.

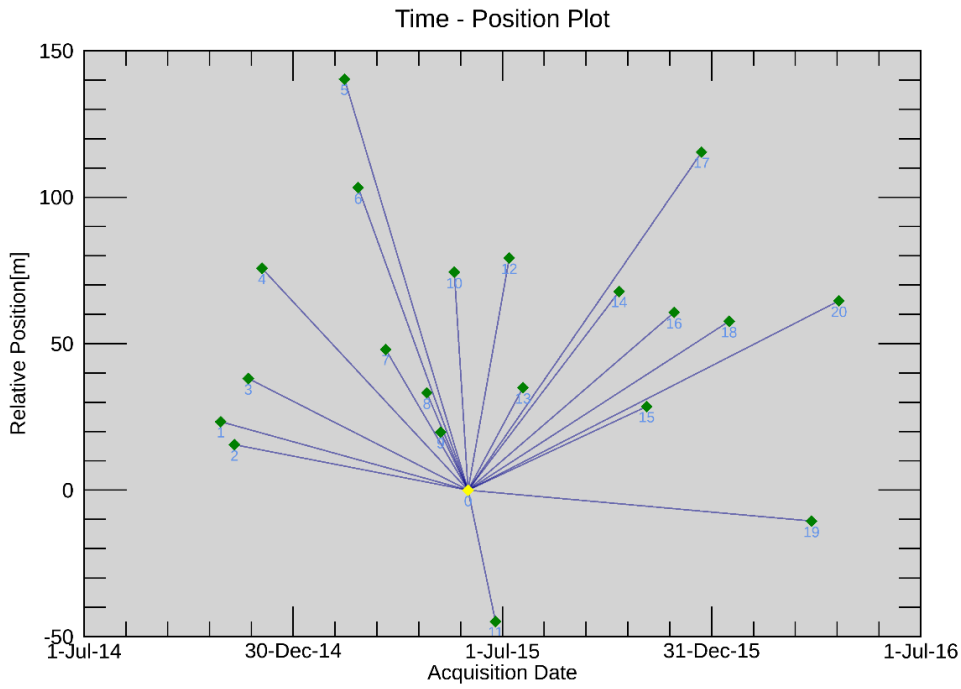


Figure 5-10: PSI time series network of slave images w.r.t. the master image shown with yellow point.

All of the images are coregistered on the master image known as Super Master image. The interferograms are generated for each slave with the same master image throughout the network. The interferograms are respectively flattened using an input reference DEM. In the following figure, the SAR intensity average image is represented which is produced from the average backscattered signals of all images in the time series network.

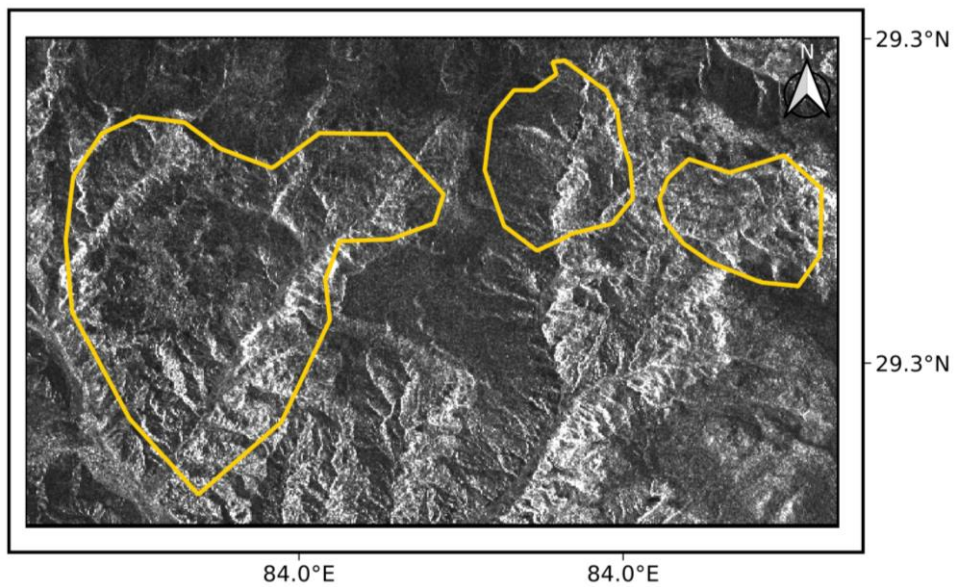


Figure 5-11: Sentinel-1 SAR intensity average image

Based on the average intensity image shown above, it is seen that some parts in the area do not reflect back the signal very well due to the slope variations. In the next step, the interferograms are created with respect to the super master image. Due to the temporal distance between the pairs, those pairs whose acquisition dates are closer to the super master date show better interferogram quality.



Figure 5-12: The generated interferograms for Sentinel-1 data w.r.t. the super master image (21.03.2015)

The multi-temporal coherence which shows how much the displacement trend fits with the PS technique model. As shown in the below figure, the bright color indicates perfect PS model match and the black color represents low or almost no model match in the study area.

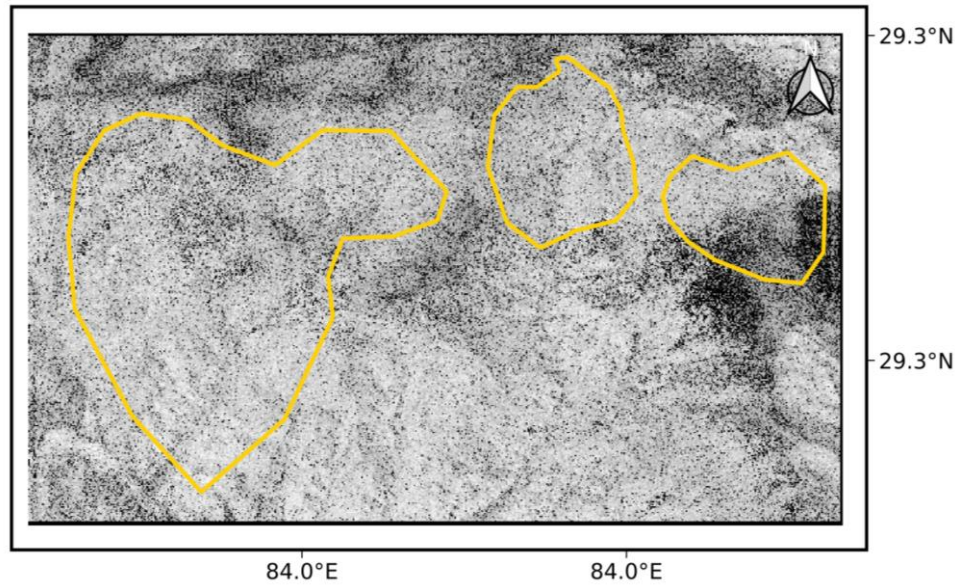


Figure 5-13: Multi-temporal coherence with white color indicating perfect PS model fit.

The derived average LOS displacement velocity maps for each of the three landslides are shown in the following figures. The pink point outside the landslide boundary points out the chosen reference point at which there has been no deformation. The reference point value has been subtracted from all the points inside the landslide boundary to convert the displacement results from an InSAR relative-based to an absolute estimated displacement values.

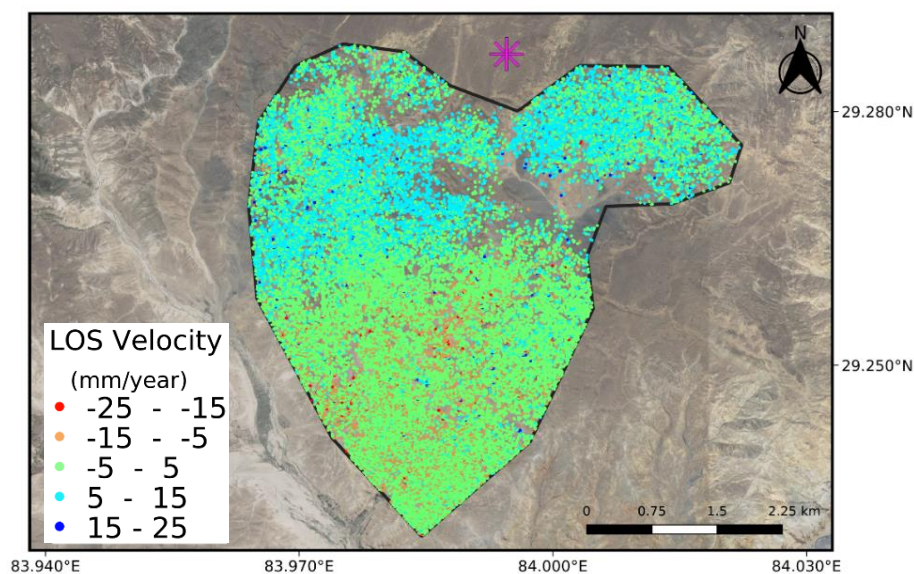


Figure 5-14: PSI average LOS displacement velocity map for the first landslide area. The unit is in mm/year.

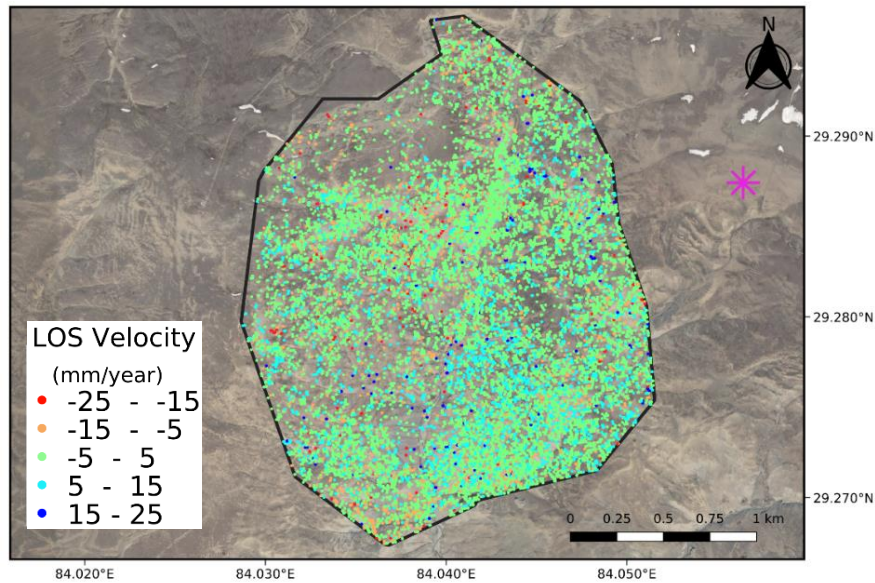


Figure 5-15: PSI average LOS displacement velocity map for the second landslide area. The unit is in mm/year.

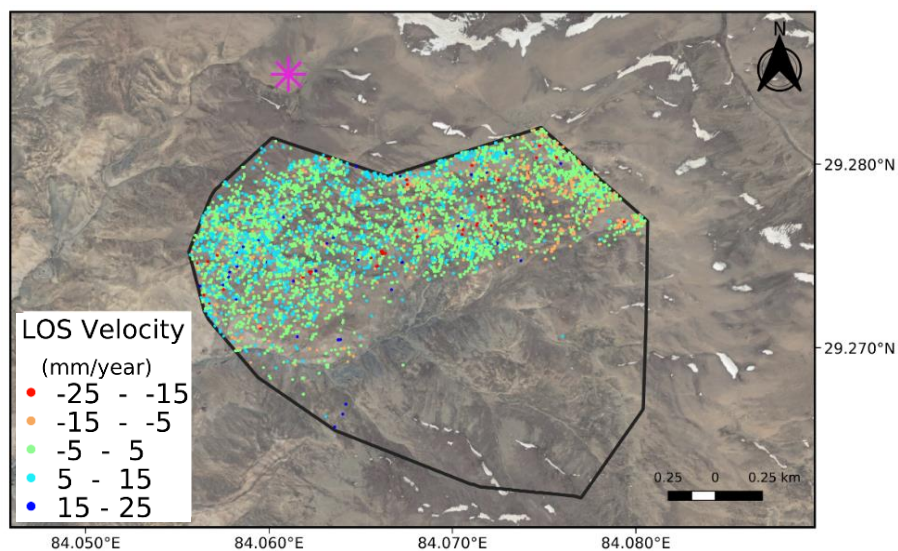


Figure 5-16: PSI average LOS displacement velocity map for the third landslide area. The unit is in mm/year.

The results of the average LOS velocity maps for both ALOS-1 and Sentinel-1 datasets could be compared to notice the differences and similarities in the following figures. It has been noticed that most of the points are obtained within the LOS velocity interval of -5 and +5 (mm per year) with 39229, 8672 and 6927 points obtained in the first, second and third landslide area of ALOS-1 and with 50093, 14236 and 4279 points in the first, second and third landslide area of Sentinel-1 data set.

It could be inferred that both datasets have nearly similar results with respect to different LOS velocity intervals. Both of them follow approximately the same trend and not a major difference is observed between them which could be shown in the following figures.

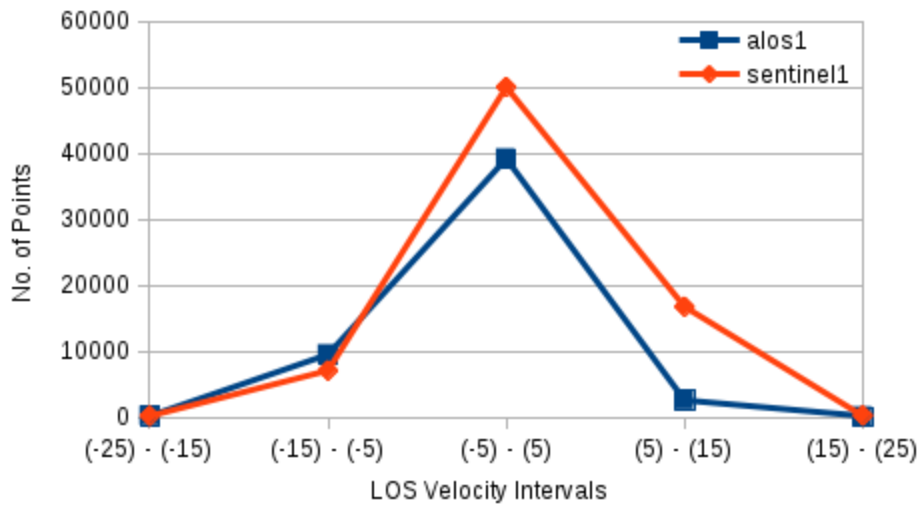


Figure 5-17: Number of points obtained in the first landslide area for every LOS velocity interval. The blue line indicates the ALOS-1 and the orange line indicates the Sentinel-1 data sets.

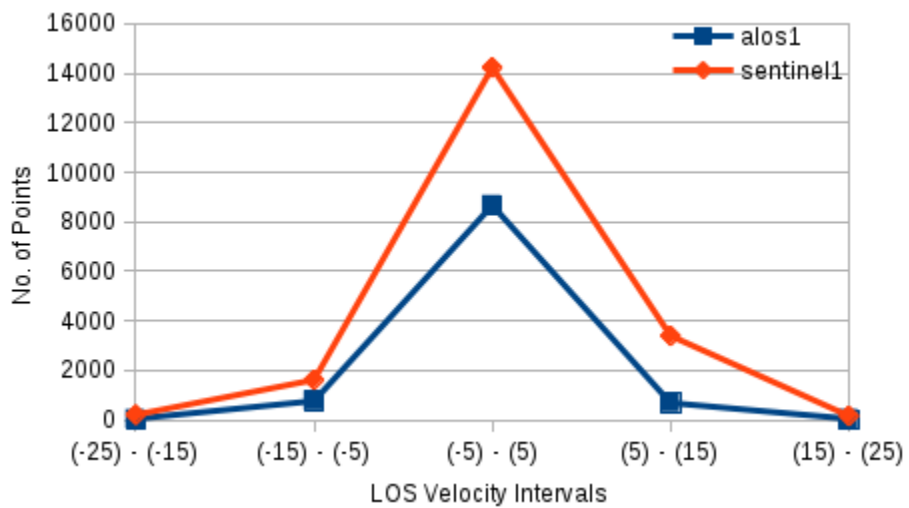


Figure 5-18: Number of points obtained in the second landslide area for every LOS velocity interval. The blue line indicates the ALOS-1 and the orange line indicates the Sentinel-1 data sets.

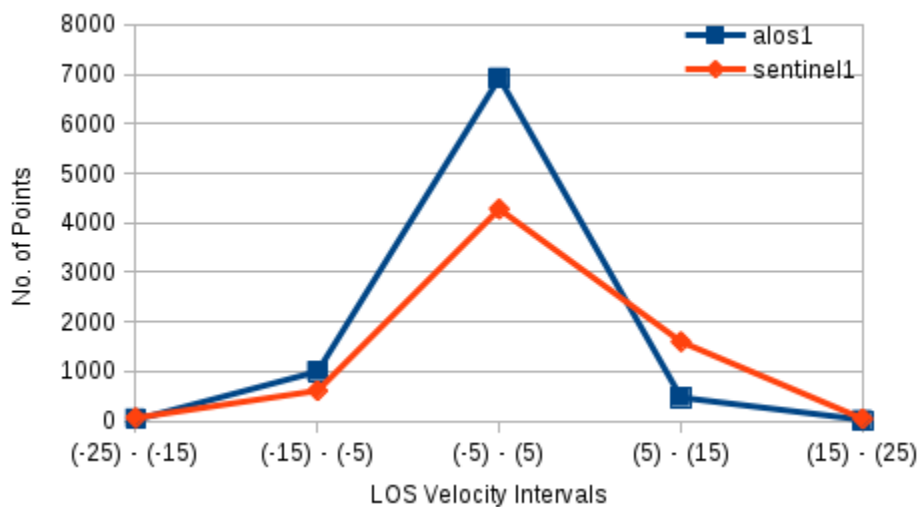


Figure 5-19: Number of points obtained in the third landslide area for every LOS velocity interval. The blue line indicates the ALOS-1 and the orange line indicates the Sentinel-1 data sets.

The obtained deformation rates based on average displacement velocity in LOS direction are further used in the post-processing strategy to extract useful information that could help identify the slow-moving landslide clusters or areas. The generated results are affected by the noise which could be mostly removed using the methodology explained further in the next chapter.

5.3 LOS Velocity Project to Slope Displacement

The Line-of-Sight average displacement velocity derived as a result of the PS time series analysis method have some challenges respect to the area's topography which consists of the mountains with high elevation with the slope's degree and direction changing frequently throughout the area. Based on the LOS values, the kinematics of the three landslide areas could not be analyzed very well as there is a need for further evaluation. Obviously, there are many derived PS points which have various average displacement velocity values due to the ground surface conditions. Therefore, the obtained LOS results need to be filtered in such a way to remove the outliers and preserve those points which represent the true ground motion.

For this purpose, the LOS displacement velocity values are projected into the slope direction considering the area's local topography and satellite's incidence and heading angle parameters. In order to project the LOS values to the slope direction, the topographic information consists of aspect and slope map which are explained in the methodology (chapter 3) of this thesis. The heading angle of the satellite in the ascending mode is equal to 352.5 degrees based on the angle from the North direction. The incidence angle of the ALOS-1 data ranges between (38.4 – 38.9) degrees and the Sentinel-1 data between (44.1 – 44.6) degrees.

The slope displacement values obtained respectively and in order to produce a high accuracy map, the points with lower sensitivity to the satellite's acquisition geometry are masked out and the points with higher sensitivity values are selected to produce the final ground surface deformation map. In the following sections, the slope displacements are shown for both datasets.

5.3.1 ALOS-1 Slope Displacement

The slope displacement values for the ALOS-1 data are obtained and as seen in the following figures, the points show a deformation rate of few to -10 millimeter per year. The positive values have been removed from the results as it is assumed the slope displacement represents downward motion. The positive values which show the motion towards the satellite's LOS direction may not be the perfectly representing the actual deformation in the study area.

As seen in the figures below, most of the slope displacement take place on the slopes to the East direction (aspect values of around 90 degrees) which the reason would be the sensitivity analysis performed on the deformation points. In fact, the slopes to the West direction are not suitable to be analyzed by ascending-mode data. In additions, it is worthy to mention that InSAR observations are in general not sensitive to the North-South direction movements.

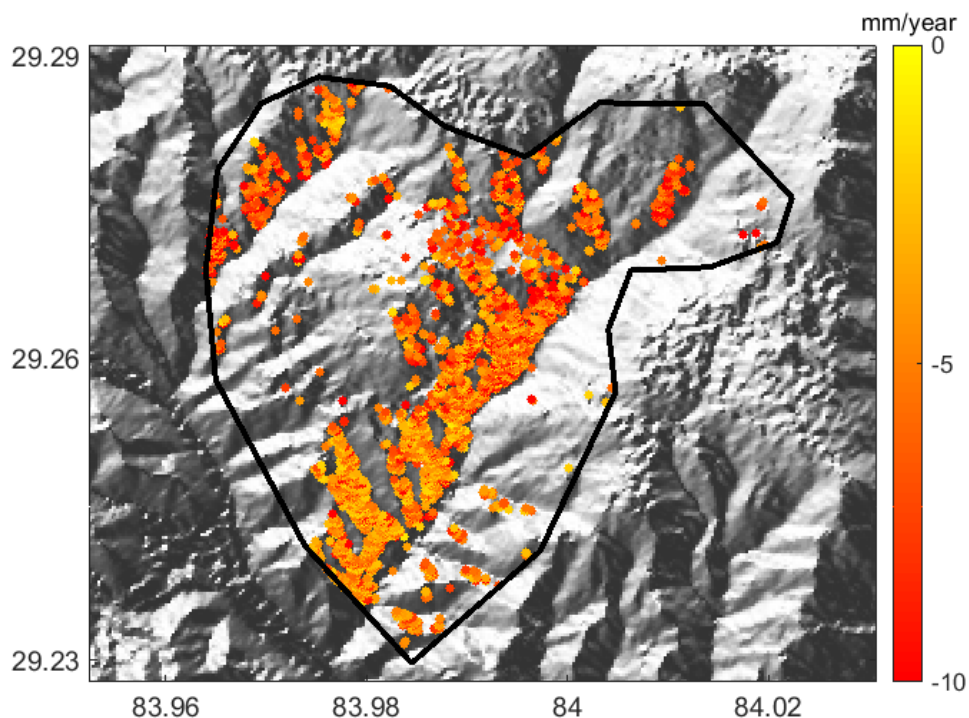


Figure 5-20: ALOS-1 slope displacement map for the first landslide area.

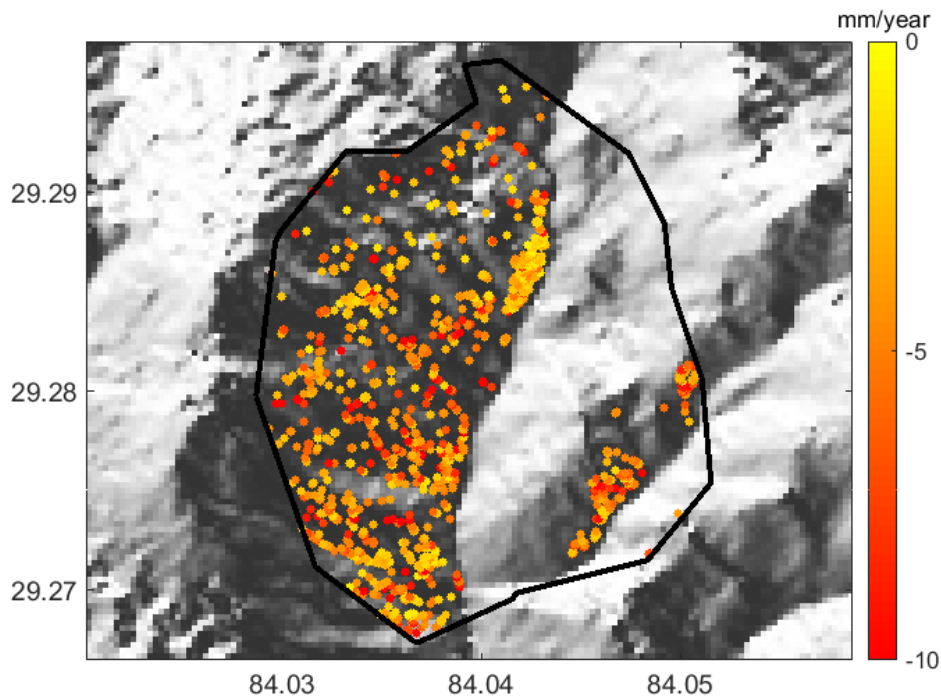


Figure 5-21: ALOS-1 slope displacement map for the second landslide area.

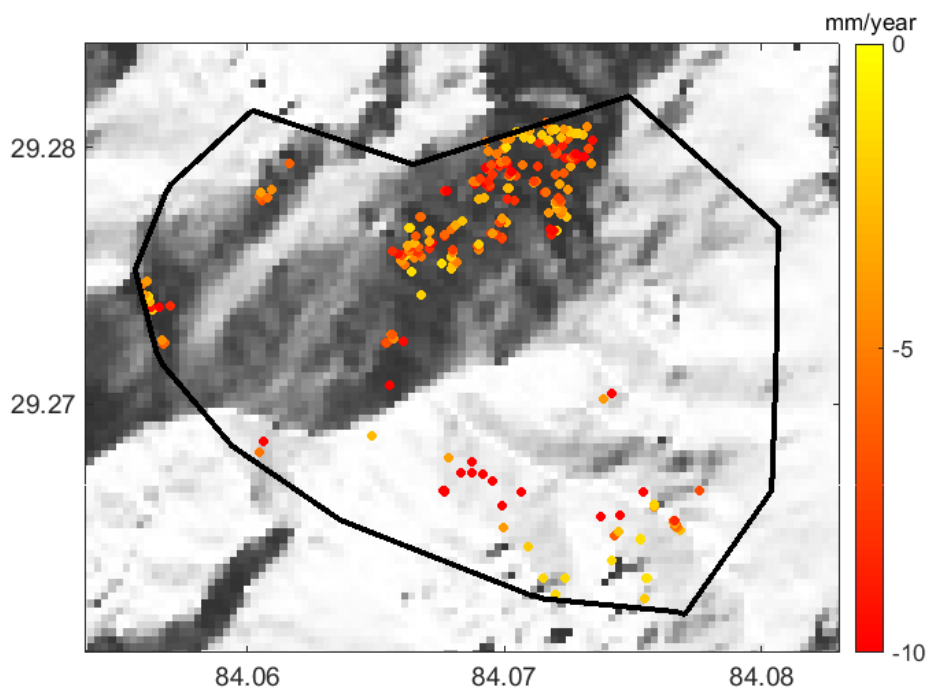


Figure 5-22: ALOS-1 slope displacement map for the third landslide area.

It is observed that many slope displacement points are obtained in the first area, whereas the third area contains the least number of points. The fact is that the slope direction in the third area is not completely compatible with the SAR's acquisition geometry as majority of the area except for the Northern part, are oriented to the West, North and South directions. In the next section, the slope displacement maps for the Sentinel-1 data set are obtained.

5.3.2 Sentinel-1 Slope Displacement

The slope displacement values for the Sentinel-1 data are obtained similarly using the same post-processing strategy as for the ALOS-1 data. The obtained velocity values show the slope displacement between the range of (0 – 10) millimeter per year after masking the positive velocity values out. Similar to ALOS-1 data, the points representing slope displacement are obtained on the slopes to the East direction once again due to the characteristics of the satellite’s acquisition geometry regarding the local topography of the study area.

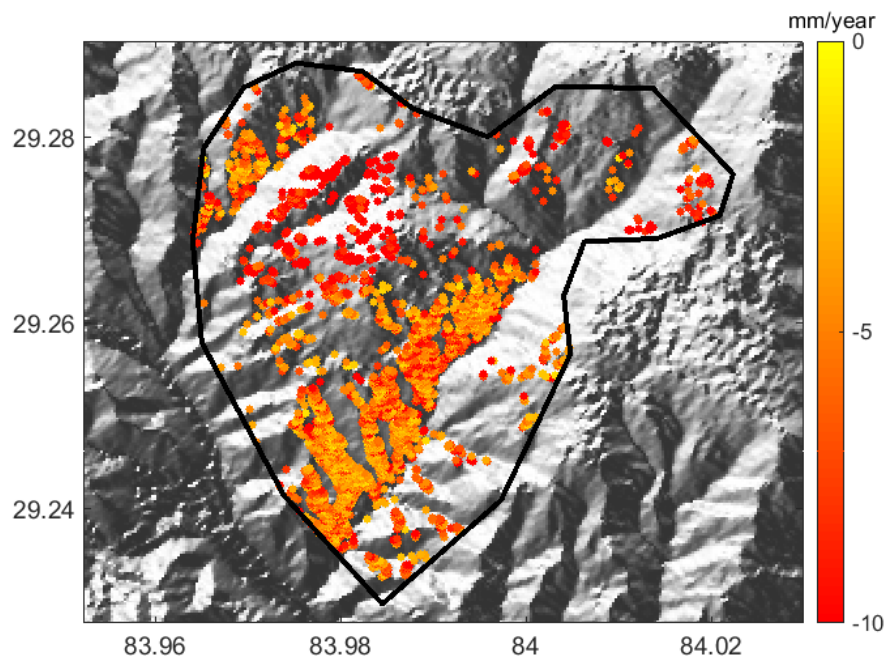


Figure 5-23: Sentinel-1 slope displacement map for the first landslide area

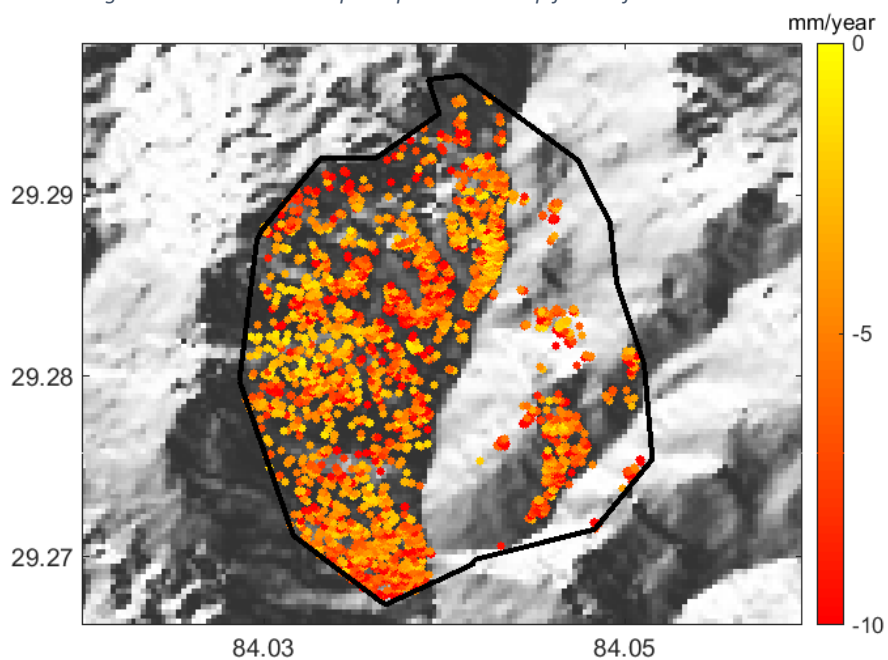


Figure 5-24: Sentinel-1 slope displacement map for the second landslide area.

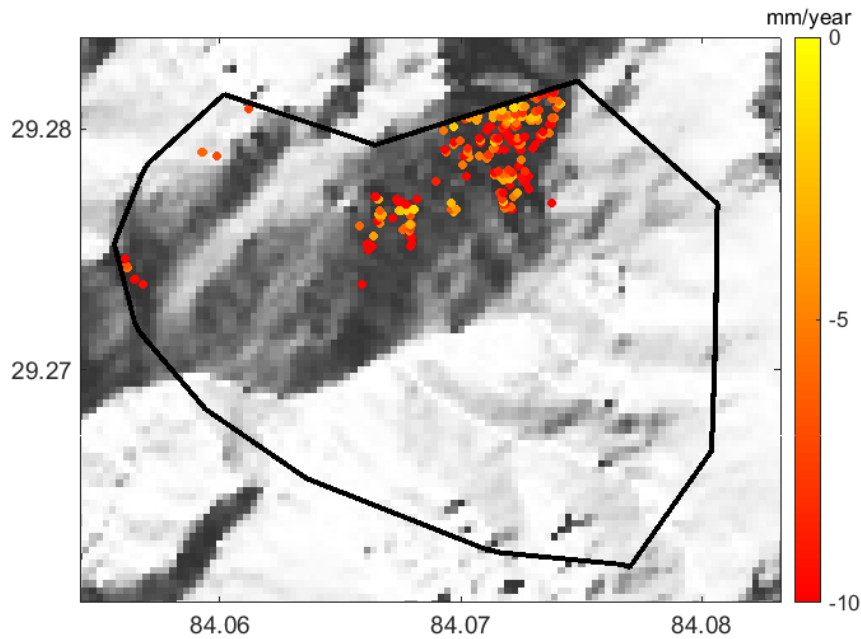


Figure 5-25: Sentinel-1 slope displacement map for the third landslide area.

After deriving the slope displacement maps for both data sets, the results derived from both of them are discussed in the following table. Overall the both data sets tend to show similar behavior as their mean velocity values are concentrated around -5 (mm/year) with the standard deviation values close to each other. There are more points in Sentinel-1 data set derived compared to the ALOS-1 one, except for the Sentinel-1 third landslide area which contains less point compared to the same area in ALOS-1 data set which also contains a higher negative mean deformation rate.

Data Set	Number of Points	Mean Velocity (mm/year)	Standard Deviation
ALOS-1 First Area	7386	-5.2	2.37
ALOS-1 Second Area	1769	-4.3	2.32
ALOS-1 Third Area	347	-5.7	2.78
Sentinel-1 First Area	9677	-5.4	2.53
Sentinel-1 Second Area	3762	-5.4	2.66
Sentinel-1 Third Area	255	-7	2.72

Table 5-3: Slope displacement comparison of three landslide areas for both ALOS-1 and Sentinel-1 data sets.

5.4 Clustering and Classification of Slope Displacement Maps

The spatial distribution of PS points in the slope displacement maps shows that the density of the PS points is relatively high especially in the first and second landslide for both

ALOS-1 and Sentinel-1 datasets. At the same time, in some areas the density of the points is very low and scattered which makes the classification of PS points more complicated. Even though the post-processing strategy has tried to remove the unnecessary points and extract the useful information out of the results, there is a need for clustering the PS points in the slope displacement maps in order to carry out the classification tasks and identify slow-moving landslides in the study area. The slow-moving landslide identification enables to detect the areas which have high probability of ground surface movement and could be used for hazard mitigation tasks.

5.4.1 Kernel Density Estimation

The Kernel Density Estimation is introduced by (Silverman, 1986) which could be used to generate kernel density maps. An approach by (Lu, Casagli, Catani, & Tofani, 2012) consists of hotspot and cluster analysis for detection of extremely slow-moving landslides in PS time series analysis. According to (Lu et al., 2012), the kernel density estimation could be calculated as:

$$f(x) = \frac{1}{nh} \sum_{i=1}^n K\left(\frac{x - X_i}{h}\right)$$

In which “h” indicates the window size, “K” as the quadratic kernel function, $(x - X_i)$ the distance of each calculating pixel to every PS target point “i”. The kernel function “K” which is a non-negative function could be further explained as below:

$$K(x) = \frac{3}{4} (1 - x^2), |x| \leq 1$$

$$K(x) = 0, x > 1$$

The kernel density estimation could be used to derive hotspots for the PS points in order to visualize clusters of points with high density. Therefore, the kernel density estimator is applied on the slope displacement maps to find high density clusters of PS points.

5.4.2 Clustering of ALOS-1 Slope Displacement Map

In the following figure, the kernel density estimation is implemented on the slope displacement map for the first landslide area, which the bright (yellow) color shows the clusters with high density PS points. Additionally, the low density clusters are removed from the final results.

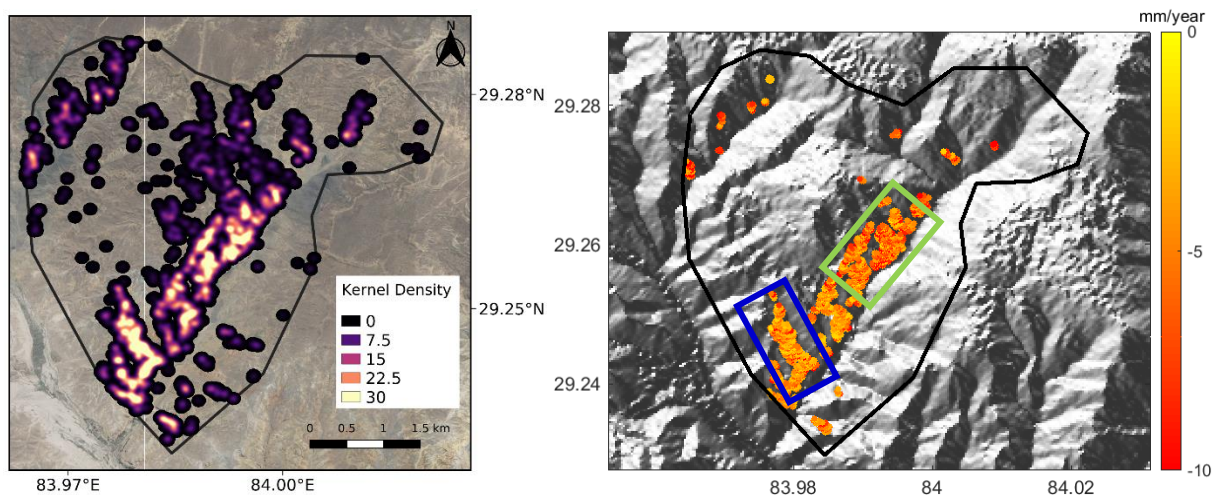


Figure 5-26: The figure on the left shows the kernel density estimation map of hotspot clusters. The clusters with high density have bright color. The figure on the right shows the slope displacement map after removing the low density cluster of points.

The two rectangles represent clusters of high density points in the slope displacement map. The deformation time series of both clusters are shown in the following figures using average time series deformation of the points in a 150 x 150 meters grid. The averaged time series of a point in the blue rectangle has an average slope displacement of -4 millimeter per year and similarly the one in the green rectangle has -8 millimeter per year value. The time series of both points are shown below.

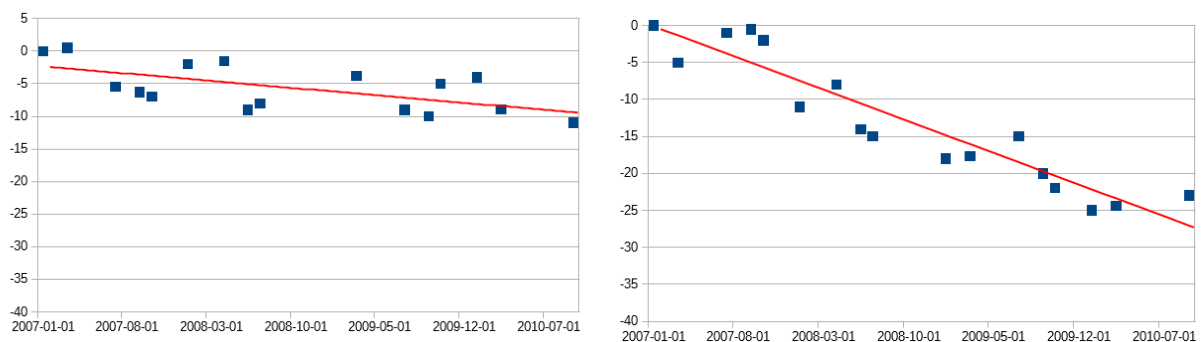


Figure 5-27: The left figure indicates the time series of a point in the blue rectangle cluster. The right figure indicates the time series of a point in the green rectangle cluster.

As could be observed from the time series plots, the point in the left cluster shows the deformation with a very slow rate and on the other side, the point in the right cluster shows a higher rate of deformation compared to the first one.

5.4.3 Clustering of Sentinel-1 Slope Displacement Map

The kernel density estimation function is implemented on the slope displacement map for the Sentinel-1 first landslide area, which the bright (yellow) color shows the clusters with high density PS points. As it is observed, most of the points in the middle part of the landslide have less density which are excluded from the final result as seen in the right below figure.

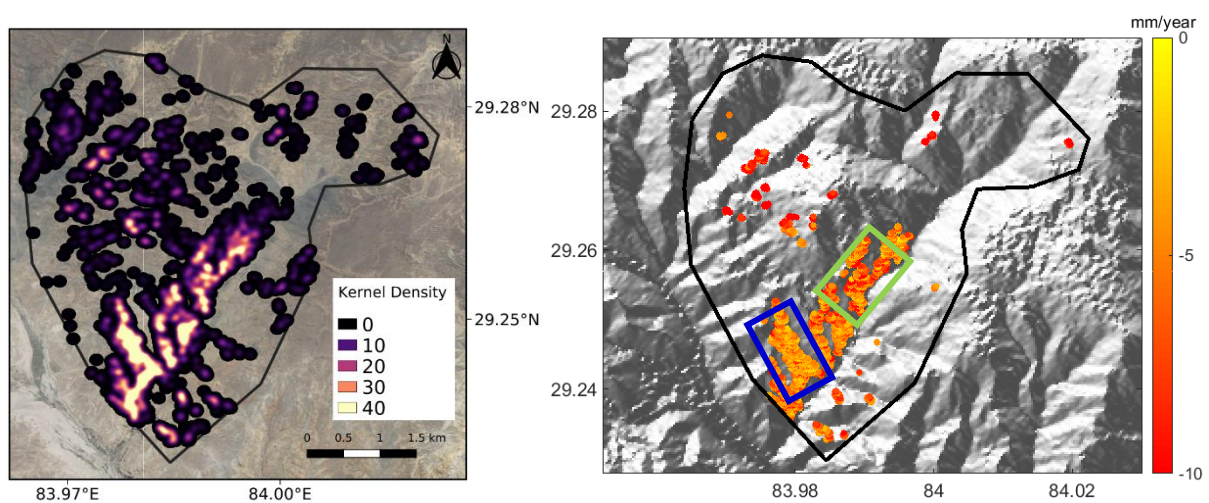


Figure 5-28: The figure on the left shows the kernel density estimation map of hotspot clusters. The clusters with high density have bright color. The figure on the right shows the slope displacement map after removing the low density cluster of points.

Similar to ALOS-1 data, here the two rectangles represent clusters of high density points in the slope displacement map. The deformation time series of both clusters are shown in the following figures using average time series deformation of the points in a 150 x 150 meters grid. The averaged time series of a point in the blue rectangle has an average slope displacement of -4.5 millimeter per year and similarly the one in the green rectangle has -9 millimeter per year value. The time series of both points are shown below.

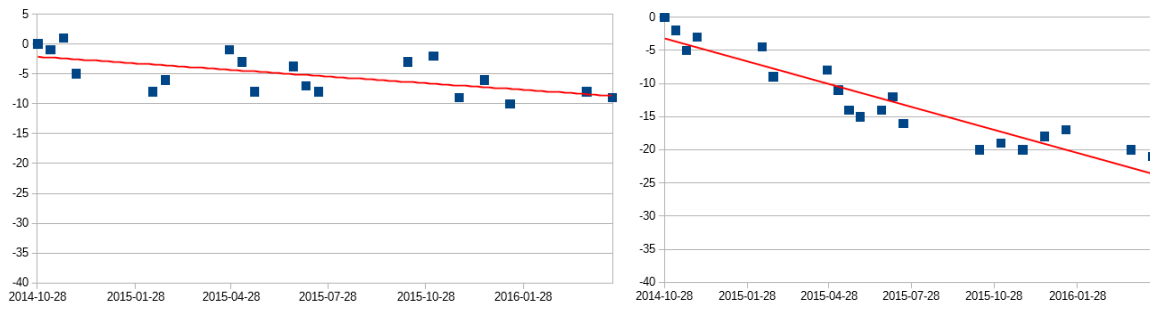


Figure 5-29: The left figure indicates the time series of a point in the blue rectangle cluster. The right figure indicates the time series of a point in the green rectangle cluster.

It has been observed from the time series plots, the point in the left cluster shows the deformation with a very slow rate and on the other side, the point in the right cluster shows a higher rate of deformation compared to the first one.

6 Conclusion and Outlook

In this thesis the aim has been to analyze the kinematics of the slow-moving landslides in northern part of Nepal. The study area consists of mountains with high slopes that makes the ground measurements difficult to an extent. At the same time, the existence of such high slopes in the mountainous regions, challenges the space geodetic techniques such as radar remote sensing observations and InSAR measurements to monitor the true ground surface movement and study the behavior of rock failure from the earth surface towards the slope direction. After having reviewed the related works from the other scientists over landslide analysis, the idea has been developed in this thesis to carry out time series analysis methods in order to analyze the landslide areas in a time interval having multiple SAR data acquired in different times.

The ALOS-1 L-band data has been used as the first data set and thanks to the availability of free Sentinel-1 data, both data sets have been used in the time series analysis. The derived average LOS displacement velocity values from PSI time series analysis method have been projected to the slope direction using topographic information such as aspect and slope values, together with satellite's acquisition geometry parameters. Using a sensitivity analysis, the points sensitive to the acquisition geometry of satellite and the local topography have been selected to create the slope displacement map which shows the deformation in the slope direction.

The slope displacement results show that the landslide areas have a deformation velocity rate of 0 to -10 millimeter per year in the slope direction. In fact, after taking into consideration of the implemented post-processing strategy, the results have been refined which indicate the optimized rate of deformation in the study area. The further step to cluster and derive the average time series of deformation has been done to illustrate the behavior of the landslide area and cluster/classify those regions that have higher density deformation points.

The SBAS time series analysis method has also been implemented on the data sets which considers those interferograms having small spatial and temporal baseline between acquisitions. The SBAS method is considered to be more stable in the non-urban areas due to

less spatial and temporal decorrelation in the interferograms, however, the obtained results from SBAS for both data sets were affected by the tropospheric errors correlated with the topography. Therefore, the atmospheric phase caused by troposphere has to be estimated and removed from the actual phase.

It could be proposed from this work to include more data in order to have a better time series network and integrate data from external sources to analyze the interferograms. The loss of coherence and interferometric fringes could be analyzed using external sources such as precipitation data, ground water level data, etc. In additions, some ground measurements and field works could help better understand the landslide processes.

7 References

- Albiol, D., Iglesias, R., Sánchez, F., & Duro, J. (2014). Improved characterization of slow-moving landslides by means of adaptive NL-InSAR filtering. *SAR Image Analysis, Modeling, and Techniques XIV*, 9243(September), 924308. <https://doi.org/10.1117/12.2067357>
- Bamler, R., & Hartl, P. (1998). Synthetic aperture radar interferometry, *14*(September), 1–55.
- Barra, A., Monserrat, O., Mazzanti, P., Esposito, C., Crosetto, M., & Scarascia Mugnozza, G. (2016). First insights on the potential of Sentinel-1 for landslides detection. *Geomatics, Natural Hazards and Risk*, *7*(6), 1874–1883. <https://doi.org/10.1080/19475705.2016.1171258>
- Berardino, P., Mora, O., Lanari, R., Sansosti, E., & Mallorqui, J. J. (2003). A new algorithm for monitoring localized deformation phenomena based on small baseline differential SAR interferograms, *40*(11), 1237–1239. <https://doi.org/10.1109/igarss.2002.1025900>
- Crosetto, M., Monserrat, O., Cuevas-González, M., Devanthéry, N., & Crippa, B. (2016). Persistent Scatterer Interferometry: A review. *ISPRS Journal of Photogrammetry and Remote Sensing*, *115*, 78–89. <https://doi.org/10.1016/j.isprsjprs.2015.10.011>
- Dai, K., Liu, G., Li, Z., Li, T., Yu, B., Wang, X., & Singleton, A. (2015). Extracting vertical displacement rates in Shanghai (China) with multi-platform SAR images. *Remote Sensing*, *7*(8), 9542–9562. <https://doi.org/10.3390/rs70809542>
- Dai, K., Xu, Q., Li, Z., Tomás, R., Fan, X., Dong, X., ... Ran, P. (2019). Post-disaster assessment of 2017 catastrophic Xinmo landslide (China) by spaceborne SAR interferometry. *Landslides*, (September 2018). <https://doi.org/10.1007/s10346-019-01152-4>
- ESA TOPS Interferometry Tutorial, I. (2015). Sentinel-1 Toolbox Interferometry Tutorial, (May 2014), 1–20.
- Ferretti, A., Fumagalli, A., Novali, F., Prati, C., Rocca, F., & Rucci, A. (2011). A new algorithm for processing interferometric data-stacks: SqueeSAR. *IEEE Transactions on Geoscience and Remote Sensing*, *49*(9), 3460–3470. <https://doi.org/10.1109/TGRS.2011.2124465>
- Ferretti, A., Prati, C., & Rocca, F. (2000). Nonlinear subsidence rate estimation using permanent scatterers in differential SAR interferometry. *IEEE Transactions on Geoscience and Remote Sensing*, *38*(5 I), 2202–2212. <https://doi.org/10.1109/36.868878>
- Ferretti, A., Prati, C., & Rocca, F. (2001). Permanent scatterers in SAR interferometry. *IEEE Transactions on Geoscience and Remote Sensing*, *39*(1), 8–20. <https://doi.org/10.1109/36.898661>
- García-Davalillo, J. C., Herrera, G., Notti, D., Strozzi, T., & Álvarez-Fernández, I. (2014). DInSAR analysis of ALOS PALSAR images for the assessment of very slow landslides: The Tena

- Valley case study. *Landslides*, 11(2), 225–246. <https://doi.org/10.1007/s10346-012-0379-8>
- Haghshenas Haghghi, M., & Motagh, M. (2016). Assessment of ground surface displacement in Taihape landslide, New Zealand, with C- and X-band SAR interferometry. *New Zealand Journal of Geology and Geophysics*, 59(1), 136–146. <https://doi.org/10.1080/00288306.2015.1127824>
- Handwerger, A. L., Booth, A. M., Huang, M.-H., Fielding, E. J., & Bürgmann, R. (2019). A shift from drought to extreme rainfall drives a stable landslide to catastrophic failure. *Scientific Reports*, 9(1), 1–12. <https://doi.org/10.1038/s41598-018-38300-0>
- Handwerger, A. L., Roering, J. J., & Schmidt, D. A. (2013). Controls on the seasonal deformation of slow-moving landslides. *Earth and Planetary Science Letters*, 377–378, 239–247. <https://doi.org/10.1016/j.epsl.2013.06.047>
- Herrera, G., Davalillo, J. C., Mulas, J., Cooksley, G., Monserrat, O., & Pancioli, V. (2009). Mapping and monitoring geomorphological processes in mountainous areas using PSI data: Central Pyrenees case study. *Natural Hazards and Earth System Science*, 9(5), 1587–1598. <https://doi.org/10.5194/nhess-9-1587-2009>
- Herrera, G., Gutiérrez, F., García-Davalillo, J. C., Guerrero, J., Notti, D., Galve, J. P., ... Cooksley, G. (2013). Multi-sensor advanced DInSAR monitoring of very slow landslides: The Tena Valley case study (Central Spanish Pyrenees). *Remote Sensing of Environment*, 128, 31–43. <https://doi.org/10.1016/j.rse.2012.09.020>
- Hilley, G. E., Bürgmann, R., Ferretti, A., Novali, F., & Rocca, F. (2004). Dynamics of slow-moving landslides from permanent scatterer analysis. *Science*, 304(5679), 1952–1955. <https://doi.org/10.1126/science.1098821>
- Hooper, A., Segall, P., & Zebker, H. (2007). Persistent scatterer interferometric synthetic aperture radar for crustal deformation analysis, with application to Volcán Alcedo, Galápagos. *Journal of Geophysical Research: Solid Earth*, 112(7), 1–21. <https://doi.org/10.1029/2006JB004763>
- Iwata, T., Ishida, H., Osawa, Y., & Tomi, K. (2003). ALOS (Advanced Land Observing Satellite). *Orbit An International Journal On Orbital Disorders And Facial Reconstructive Surgery*, 23(1), 16.
- Lu, P., Casagli, N., Catani, F., & Tofani, V. (2012). Persistent scatterers interferometry hotspot and cluster analysis (PSI-HCA) for detection of extremely slow-moving landslides. *International Journal of Remote Sensing*, 33(2), 466–489. <https://doi.org/10.1080/01431161.2010.536185>
- Mirzaee, S., Motagh, M., & Akbari, B. (2017). Landslide monitoring using insar time-series and GPS observations, case study: Shabkola landslide in northern Iran. *International Archives of the Photogrammetry, Remote Sensing and Spatial Information Sciences - ISPRS Archives*, 42(1W1), 487–492. <https://doi.org/10.5194/isprs-archives-XLII-1-W1-487-2017>

- Mirzaee, S., Motagh, M., Akbari, B., Wetzel, H. U., & Roessner, S. (2017). EVALUATING THREE INSAR TIME-SERIES METHODS to ASSESS CREEP MOTION, CASE STUDY: MASOULEH LANDSLIDE in NORTH IRAN. *ISPRS Annals of the Photogrammetry, Remote Sensing and Spatial Information Sciences*, 4(1W1), 223–228. <https://doi.org/10.5194/isprs-annals-IV-1-W1-223-2017>
- Mochammad, M., & Saepuloh, A. (2017). Analyses of surface deformation with SBAR InSAR method and its relationship with aquifer occurrence in Surabaya City, East Java, Indonesia. *IOP Conference Series: Earth and Environmental Science*, 71(1). <https://doi.org/10.1088/1755-1315/71/1/012010>
- Moretti, S., Mora, O., Mateos, R., Garcia, I., Notti, D., Herrera, G., & Bianchini, S. (2013). Landslide Activity Maps Generation by Means of Persistent Scatterer Interferometry. *Remote Sensing*, 5(12), 6198–6222. <https://doi.org/10.3390/rs5126198>
- Motagh, M., Molodbekov, B., Roessner, S., Echtler, H., Wetzel, H.-U., & Teshebaeva, K. (2015). ALOS/PALSAR InSAR Time-Series Analysis for Detecting Very Slow-Moving Landslides in Southern Kyrgyzstan. *Remote Sensing*, 7(7), 8973–8994. <https://doi.org/10.3390/rs70708973>
- Notti, D., Davalillo, J. C., Herrera, G., & Mora, O. (2010). Assessment of the performance of X-band satellite radar data for landslide mapping and monitoring: Upper Tena Valley case study. *Natural Hazards and Earth System Science*, 10(9), 1865–1875. <https://doi.org/10.5194/nhess-10-1865-2010>
- Piacentini, D., Devoto, S., Mantovani, M., Pasuto, A., Prampolini, M., & Soldati, M. (2015). Landslide susceptibility modeling assisted by persistent scatterers interferometry (PSI): An example from the northwestern coast of Malta. *Natural Hazards*, 78(1), 681–697. <https://doi.org/10.1007/s11069-015-1740-8>
- Podest, E. (2017). Basics of Synthetic Aperture Radar (SAR). Retrieved from https://arset.gsfc.nasa.gov/sites/default/files/water/Brazil_2017/Day1/S1P2.pdf
- Rott, H., Scheuchl, B., Siegel, A., & Grasemann, B. (1999). Monitoring very slow slope movements by means of SAR interferometry: A case study from a mass waste above a reservoir in the Otztal Alps, Austria. *Geophysical Research Letters*, 26(11), 1629–1632. <https://doi.org/10.1029/1999GL900262>
- Sandwell, D. T., Myer, D., Mellors, R., Shimada, M., Brooks, B., & Foster, J. (2008). Accuracy and resolution of ALOS interferometry: Vector deformation maps of the father's day intrusion at Kilauea. *IEEE Transactions on Geoscience and Remote Sensing*, 46(11), 3524–3534. <https://doi.org/10.1109/TGRS.2008.2000634>
- SARscape User Guide. (2014). SARscape Help Manual. Retrieved from https://www.harrisgeospatial.com/docs/pdf/sarscape_5.1_help.pdf
- Silverman, B. W. (1986). Density Estimation for Statistics and Data Analysis. *Monographs on Statistics and Applied Probability*, London: Chapman and Hall.

- Snoeij, P., Attema, E., Davidson, M., Duesmann, B., Floury, N., Levrini, G., ... Rosich, B. (2010). Sentinel-1 radar mission: Status and performance. *IEEE Aerospace and Electronic Systems Magazine*, 25(8), 32–39. <https://doi.org/10.1109/MAES.2010.5552610>
- Wempen, J. M., & McCarter, M. K. (2017). Comparison of L-band and X-band differential interferometric synthetic aperture radar for mine subsidence monitoring in central Utah. *International Journal of Mining Science and Technology*, 27(1), 159–163. <https://doi.org/10.1016/j.ijmst.2016.11.012>
- Xia, Y. (2010). Synthetic aperture radar interferometry. *Sciences of Geodesy - I: Advances and Future Directions*, 88(3), 415–474. https://doi.org/10.1007/978-3-642-11741-1_11